THE ASTROPHYSICAL JOURNAL, **349**:296–312, 1990 January 20

# H0534−581: A NEW INTERMEDIATE POLAR?

D. A. H. BUCKLEY AND I. R. TUOHY
Mount Stromlo and Siding Spring Observatories, Institute of Advanced Studies, Australian National University

*Received 1989 January 23; accepted 1989 July 13*

## ABSTRACT

Optical spectroscopic and photometric observations of the hard X-ray–emitting *HEAO 1* cataclysmic variable, H0534−581, are presented and interpreted. Two spectroscopic periods are identified at ~6 and 2.1 hr from measurements of the emission-line radial velocities, which we conclude are the orbital and white dwarf spin periods, respectively.

The spin-modulated velocity curves of the narrow and broad emission components are ~180° out of phase, and the latter has a larger $K$ velocity and more negative $\gamma$ velocity. Radial velocity curves of the profile wings, determined using a double Gaussian convolution method, indicate that there is a smooth variation in the curve parameters ($K$ velocity, $\gamma$ velocity, and phase) from the core-dominated regions of the profile into the wings. Magnetospheric disruption of the accretion disk close to the white dwarf ($\sim 10$–$20 R_1$), followed by forced corotation, spiral streaming, and pseudoradial infall in an accretion funnel, is the mechanism we use to explain the velocity and line profile behavior. The derived mass function of $\sim 5 \times 10^{-3}\ M_\odot$ implies that the orbital inclination is certainly less than 40°, and probably less than 26°, for an empirically derived (from $P_{\rm orb}$) secondary star mass of $\sim 0.6\ M_\odot$. An upper limit estimate of the inner disk radius is equated to the magnetospheric radius to derive an estimated surface magnetic field strength of less than 6 MG for $M_1 < 1\ M_\odot$.

A time series analysis of extensive *UBVRI* and high-speed photometry has resulted only in the identification of the orbital period (6.5 hr) and two puzzling but reasonably persistent periods at 2707 and 1938 s, neither of which can be explained adequately in terms of fundamental periods or sidebands. Reanalysis of *EXOSAT* time series data has revealed the possible presence of the 2.1 hr spin period, with pulse fractions of 17% and 36%, respectively, for the 2–6 keV (ME) and 0.1–2 keV (LE1) bands.

These results indicate that H0534−581 is a new member of the *intermediate polar* (or DQ Herculis) class of magnetic cataclysmic binaries. This is supported by the observed second radial velocity period, the extreme hardness of the X-ray spectrum ($kT > 30$ keV), a large $L_x/L_{\rm opt}$ of ~5, and the presence of strong He II λ4686 emission. The Balmer decrement indicates a central disk/magnetosphere temperature of $\sim 10^5$ K.

*Subject headings:* stars: binaries — stars: dwarf novae — stars individual (H0534−581) — stars: magnetic — X-rays: binaries

## I. INTRODUCTION

In an earlier paper (Tuohy *et al.* 1986, hereafter Paper I) we identified the hard *HEAO 1* X-ray source H0534−581 with a high-excitation cataclysmic variable (CV). We reported the results of a time series analysis on both X-ray and optical photometry which failed to detect conclusively any persistent strong periodicities. Our conclusions were that the system was either a nova-like CV or possibly an *intermediate polar* magnetic CV (also known as a DQ Herculis system) with low X-ray and optical pulse fractions.

Intermediate polars are magnetic CVs with asynchronously rotating white dwarf primaries. Accretion occurs in a column or curtain over a limited area of the white dwarf's surface, which results in a shock and subsequent cooling by hard bremsstrahlung emission with a characteristic temperature $kT > 10$ keV (for reviews see, for example, Lamb 1983, 1985; Wickramasinghe 1988). The rotation of the white dwarfs leads to energy-dependent, modulated X-ray emission at the rotation (spin) period. These systems are also characterized by optical photometric variations at several periods, dominantly at the spin period or its orbital sideband (beat) period (e.g., Warner 1983, 1986). Recent observations of intermediate polars with *EXOSAT* have also revealed multiple X-ray periods, including the orbital and beat period (e.g., Paper I; McHardy *et al.* 1987). These have been explained in terms of X-ray reflection (Buckley and Tuohy 1989), a secondary source of X-rays at the accretion stream/magnetosphere interface (McHardy *et al.* 1987), and amplitude modulation as a result of accretion "gating" (Lamb and Mason 1989).

Another observational characteristic of some intermediate polars is periodic low-amplitude spin-modulated radial velocity variations (Penning 1985; Buckley and Tuohy 1989; Chiapetti *et al.* 1989). This has been interpreted in the first two references as resulting from a beam illuminating a spot on the accretion disk or magnetospheric disruption and forced corotation of the inner disk material, respectively. The current debate on magnetic field strengths in intermediate polars (e.g., King, Frank, and Ritter 1985; Hamuery, Ling, and Lasota 1986; Lamb and Melia 1987) could be resolved by observational evidence for the presence of disks in these systems (e.g., Hellier *et al.* 1987, Buckley 1988), which limit the size of the magnetospheric radius. Equating the inner disk and magnetospheric radii leads to an estimate of the surface magnetic field strength of the white dwarf.

In this paper, we present time-resolved spectroscopic observations and high-speed optical photometry of H0534−581. In light of the spectroscopic results, in particular the radial velocity periods, we have analyzed the *EXOSAT* data and the combined photometry data (*UBVRI* and high-speed) and conclude that the system is probably a new intermediate polar with an

TABLE 1

LOG OF H0534−581 OBSERVATIONS

| Date | Duration (hr) | Telescope | Instrument | Coverage |
|---|---|---|---|---|
| | | Spectroscopy | | |
| 1985 Jan 16 | 2.5 | AAT 3.9 m | RGO + IPCS | λλ3960–5013 |
| 1985 Jan 17 | 7 | AAT 3.9 m | RGO + IPCS | λλ3960–5013 |
| 1985 Nov 17 | 0.6 | AAT 3.9 m | RGO + IPCS<br>FORS | λλ3930–4960<br>λλ5300–11000 |
| | | Photometry | | |
| 1984 Oct 24 | 2 | SSO 1.0 m | TCC | *UBVRI* |
| 1984 Nov 17 | 3.5 | SSO 1.0 m | TCC | *UBVRI* |
| 1984 Nov 18 | 4.7 | SSO 1.0 m | TCC | *UBVRI* |
| 1985 Jan 23 | 8 | SSO 2.3 m | High speed | *B* |
| 1985 Jan 24 | 2 | SSO 2.3 m | High speed | *B* |
| 1985 Nov 11 | 4 | SSO 1.0 m | TCC | *UBVRI* |
| 1986 Feb 12 | 6 | SSO 2.3 m | High speed | *B* |
| 1986 Feb 14 | 6 | SSO 2.3 m | High speed | *B* |
| 1986 Feb 15 | 6 | SSO 2.3 m | High speed | *B* |

orbital period of ~6.5 hr and a spin period of 2.1 hr, the longest yet found for such a system.

## II. SPECTROSCOPY

### *a*) *Observations*

Time-resolved spectroscopy was undertaken of H0534−581 on 1985 January 16 and 17 and November 17 using the RGO spectrograph with the IPCS on the 3.9 m Anglo-Australian Telescope (AAT). A log of the observations is presented in Table 1. The instrumental setup was essentially the same as described for 1H0542−407 in Paper II (Buckley and Tuohy 1989). For the 1985 January observations, the wavelength coverage was 3950–5010 Å with a resolution of ~1.3 Å. Only ~2.5 hr of data were obtained on the first night, due to the presence of cloud, in seeing conditions which varied between 1″.5 and 4″. On the second night, which was cloudless, we obtained ~7 hr of data in poor seeing, ranging from ~3″ at the start of the night to 8″ by the end. Approximately 1 hr of data were obtained on November 17 in two spectral regions, 3930–4960 Å and 5300–11000 Å, simultaneously. The same RGO/IPCS combination was used for the former, while the latter data were obtained using the low-resolution (~20 Å) faint object red spectrograph (FORS).

For all the IPCS observations, the continuous high-speed mode of operation was employed (e.g., Watts *et al.* 1986; Paper II). The original integration time was chosen to be 300 s, although later the spectra were rebinned to 900 s to improve the signal-to-noise ratio. Spectra were also taken approximately every half hour of a Cu-Ar comparison arc to enable wavelength calibration and monitoring of instrumental shifts. Subsequent cross correlations performed on these 14 spectra showed them to be stable to a few km $s^{-1}$. Only the spectra for January 17 were fluxed calibrated.

In Figure 1*a*, we show the calibrated grand-sum spectrum, uncorrected for velocity variations, obtained on 1985 January 17. It is very similar to our spectrum of 1984 October 19 (Paper I). The limited observations conducted on 1985 November 17 resulted in a single, uncalibrated red spectrum (λλ5300–11000), which is shown in Figure 1*b*. It shows the presence of the Paschen series and He I lines, but no evidence for secondary

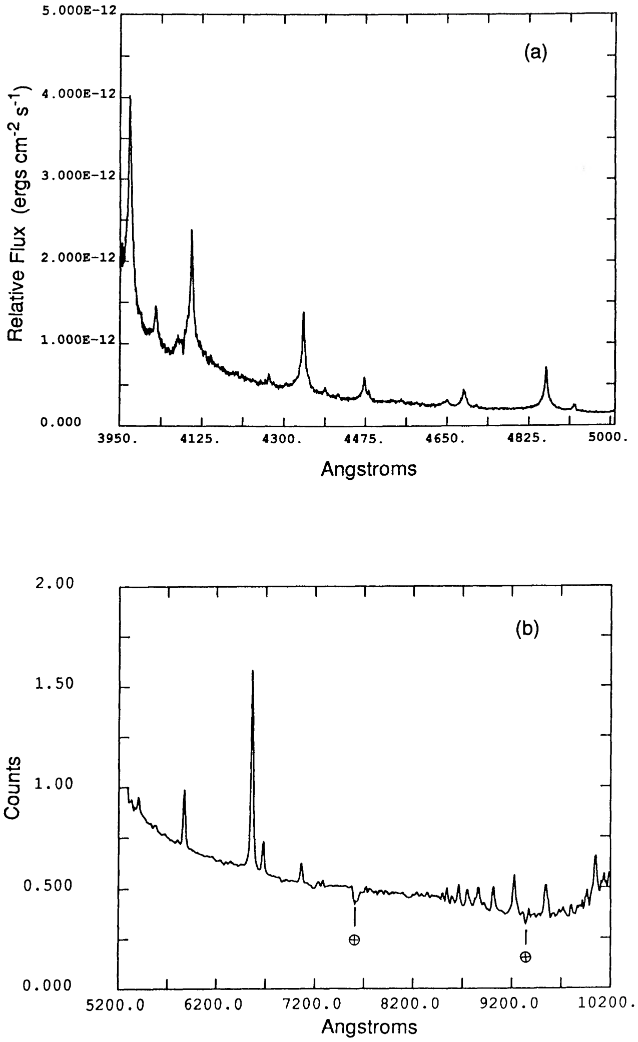

FIG. 1.—(*a*) Summed blue spectrum (IPCS) of H0534−581 taken on 1985 January 17 with the AAT. No radial velocity corrections have been applied. (*b*) Red spectrum (FORS) of H0534−581 taken on 1985 November 17 with the AAT. Residual atmospheric absorption features are marked with a "⊕."

star features, for example the Na I doublet λλ8183, 8195, the Ca II triplet λλ8498, 8542, 8662, or the TiO band heads at λλ7170, 7600. However, we emphasize the low resolution (~20 Å) of these red spectra.

### *b) Emission-Line Profiles and Velocities*

We adopted the technique described in Paper II to fit Gaussian profiles to the emission lines in H0534−581. A satisfactory fit was achieved using two Gaussians for each line, of FHWM ~300 and 1100 km s$^{-1}$. We also experimented with fitting Lorentzian wings and a Gaussian core to the lines, which gave similar results. The Gaussian had a FWHM of ~300 km s$^{-1}$, while the FWHM of the Lorentzian was ~1500 km s$^{-1}$. Both types of fit represented the observed profiles well, with the residuals of the latter Gaussian-Lorentzian fit only slightly improved in the region 200–400 km s$^{-1}$ from line center.

The variations of the velocity, sigma (or FWHM), equivalent width, and amplitude of the narrower Gaussian component

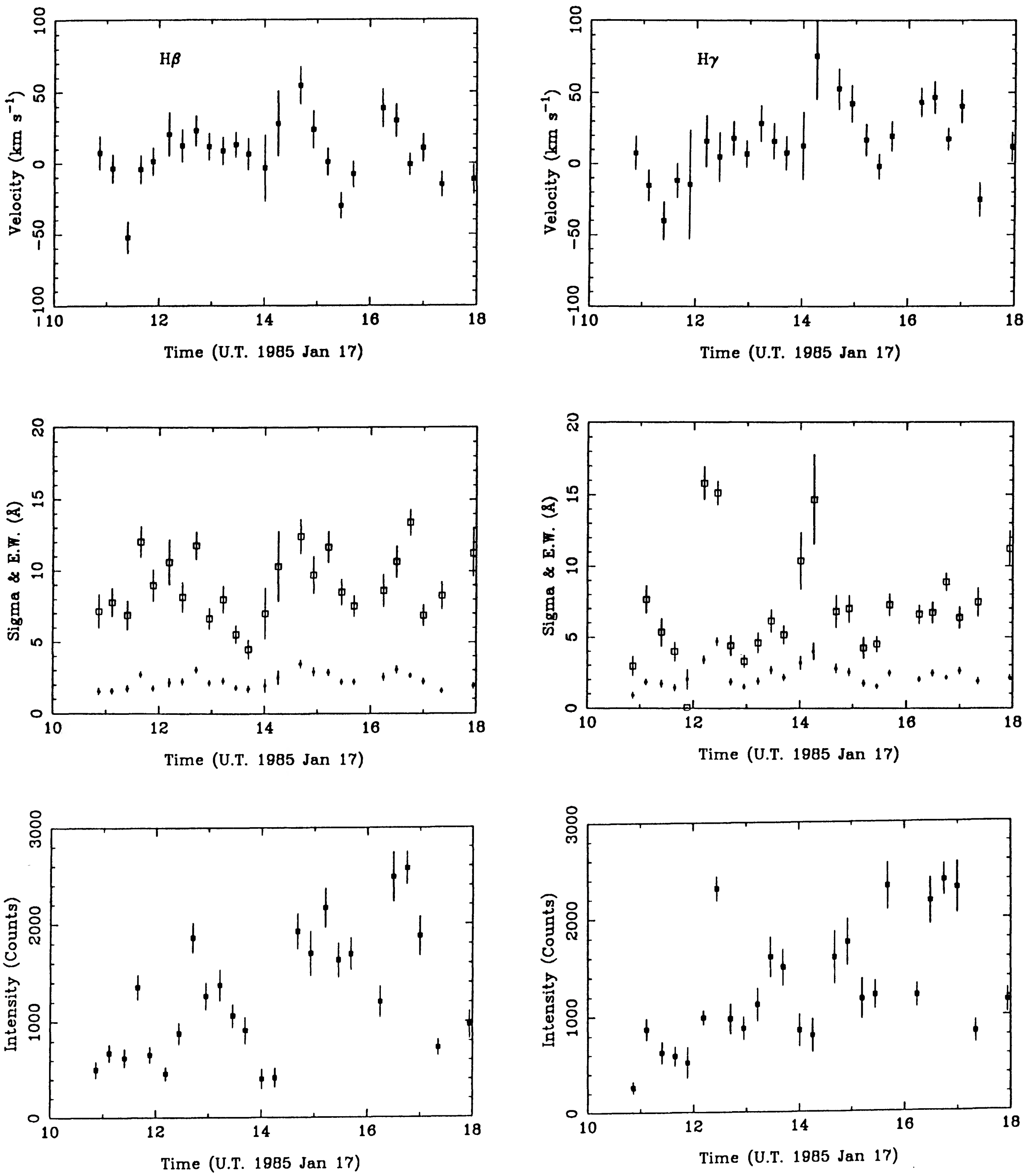

FIG. 2.—Variations of the radial velocity, sigma, equivalent width, and intensity of the narrower Gaussian component of Hβ and Hγ on 1985 January 17. Sigma points are the filled squares (■) in the lower part of the middle panels.

TABLE 2

Emission Line Parameters

| Line | Flux (ergs cm$^{-2}$ s$^{-1}$) | E.W. (Å) | FWHM (km s$^{-1}$) |
|---|---|---|---|
| H$\epsilon$ (narrow) .............. | $5.59 \pm 0.73 \times 10^{-14}$ | $2.67 \pm 0.35$ | $332 \pm 23$ |
| H$\epsilon$ (wide .................. | $1.91 \pm 0.08 \times 10^{-13}$ | $9.12 \pm 0.36$ | $1018 \pm 52$ |
| H$\delta$ (narrow) ............. | $1.02 \pm 0.06 \times 10^{-13}$ | $5.67 \pm 0.33$ | $372 \pm 16$ |
| H$\delta$ (wide) ................ | $2.56 \pm 0.11 \times 10^{-13}$ | $14.24 \pm 0.62$ | $1791 \pm 85$ |
| H$\gamma$ (narrow) .............. | $6.78 \pm 0.32 \times 10^{-14}$ | $5.74 \pm 0.27$ | $333 \pm 11$ |
| H$\gamma$ (wide) ................. | $2.00 \pm 0.05 \times 10^{-13}$ | $16.91 \pm 0.41$ | $1485 \pm 42$ |
| H$\beta$ (narrow) ............. | $5.63 \pm 0.18 \times 10^{-14}$ | $8.17 \pm 0.26$ | $321 \pm 8$ |
| H$\beta$ (wide) ................ | $1.51 \pm 0.03 \times 10^{-13}$ | $21.95 \pm 0.44$ | $1530 \pm 35$ |
| He I $\lambda$4471 (narrow) ..... | $1.91 \pm 0.14 \times 10^{-14}$ | $2.1 \pm 0.2$ | $282 \pm 16$ |
| He I $\lambda$4471 (wide) ........ | $6.65 \pm 0.28 \times 10^{-14}$ | $7.3 \pm 0.3$ | $1345 \pm 57$ |
| Mg II $\lambda$4481 .............. | $4.8 \pm 0.8 \times 10^{-15}$ | $0.54 \pm 0.09$ | $182 \pm 27$ |
| C III–N III $\lambda$4650 ........ | $2.76 \pm 0.20 \times 10^{-14}$ | $3.63 \pm 0.26$ | $1036 \pm 71$ |
| He II $\lambda$4686 .............. | $7.03 \pm 0.17 \times 10^{-14}$ | $9.44 \pm 0.23$ | $794 \pm 19$ |

(FWHM ~300 km s$^{-1}$) for the strong lines H$\beta$ and H$\gamma$ are plotted in Figure 2. In Table 2, the mean values for the line flux, equivalent width, and FWHM are given for both the narrow and wide Gaussian components of the Balmer, He I $\lambda$4471 and He II $\lambda$4686 lines in the averaged spectrum for 1985 January 17. Most noticeable in Figure 2 is a quasi-sinusoidal variation in the emission-line parameters with a period of ~2 hr.

To confirm the presence of this variation, we used a cross-correlation technique on various combinations of lines. First, we "flattened" the continuum by low-frequency filtering and applied a high-frequency cosine-bell cutoff. We experimented with several subsets of spectral data, some with all the Balmer lines present (H$\epsilon$, H$\delta$, H$\gamma$, and H$\beta$), and the He I and He II lines replaced by a pseudocontinuum, others with just two Balmer lines (e.g., H$\delta$ and H$\gamma$, H$\gamma$ and H$\beta$), and one with only the He II $\lambda$4686 line. The results were that in all cases we confirmed velocity variations at periods ~2 and 5–7 hr. Errors in the velocity determinations were reduced considerably for cross correlations of the multiple line sets; for example, the Balmer lines (Fig. 3*a*). To facilitate a study of the line wings (§ II*d*), we decided to improve the signal-to-noise ratio of the spectra by rebinning the data into 10 approximately equally spaced phase bins. These spectra were reanalyzed by profile fitting and cross-correlation, resulting in new velocities entirely consistent with the previous results, while having less scatter for the weaker lines of He I and He II $\lambda$4686.

### *c) Radial Velocity Curves*

A $\chi^2$ minimization procedure was used to fit two sine curves to the various sets of velocity data obtained on 1985 January 17. The function was of the form

$$V(t) = \gamma + K_1 \sin 2\pi\left(\frac{t - T_1}{P_1}\right) + K_2 \sin 2\pi\left(\frac{t - T_2}{P_2}\right) . \quad (1)$$

The values of the parameters are given in Table 3, while the fits to the Balmer velocity curves can be seen in Figures 3*a*–3*c*. A value of $2.1 \pm 0.1$ hr was obtained for the shorter period, while the longer period is less well constrained at $6.5 \pm 1.0$ hr. We

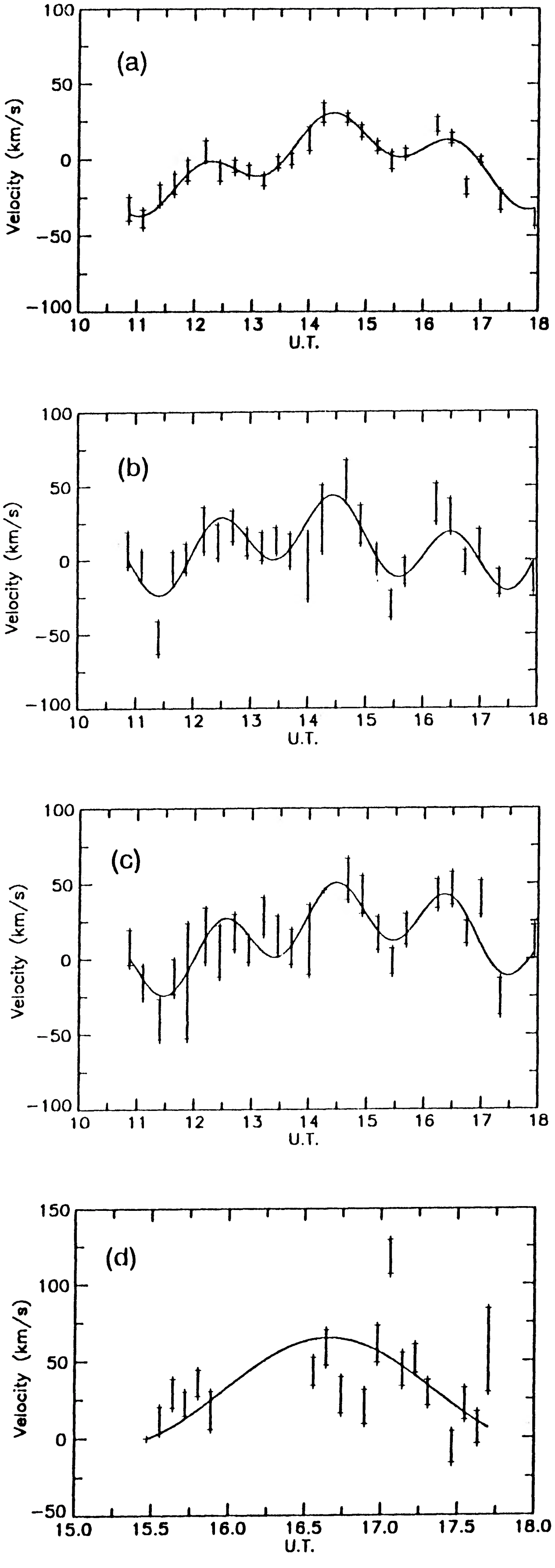

Fig. 3.—Sinusoidal fits to the emission-line radial velocities: for the cross-correlation velocities of the Balmer lines (*a*) for the core Gaussian component velocities for H$\beta$ (*b*) and H$\gamma$ (*c*); all on 1985 January 17, and Balmer cross correlation velocities on 1985 January 16 (*d*).

TABLE 3

RADIAL VELOCITY PARAMETERS

| Line | $\gamma$ (km s$^{-1}$) | $K_1$ (km s$^{-1}$) | $T_1$ (U.T.) | $P_1$ (hr) | $K_2$ (km s$^{-1}$) | $T_2$ (UT) | $P_2$ (hr) |
|---|---|---|---|---|---|---|---|
| Hδ, Hγ, Hβ[a] ..... | 1.3 ± 3.9 | 11.4 ± 5.7 | 16.01 ± 0.18 | 2.17 ± 0.17 | ... | ... | ... |
| | −2.6 ± 4.1 | 13.0 ± 2.5 | 16.05 ± 0.07 | 2.23 ± 0.07 | 21.5 ± 3.4 | 12.90 ± 0.30 | 7.53 ± 1.13 |
| Hβ ............... | 6.3 ± 4.2 | 18.4 ± 5.7 | 16.00 ± 0.13 | 2.01 ± 0.08 | ... | ... | ... |
| | 10.5 ± 4.4 | 20.8 ± 4.6 | 16.01 ± 0.09 | 2.04 ± 0.07 | 13.7 ± 5.2 | 12.66 ± 0.48 | 5.6 ± 1.11 |
| Hγ ............... | 17.1 ± 4.7 | 20.0 ± 6.5 | 15.96 ± 0.12 | 2.05 ± 0.09 | ... | ... | ... |
| | 12.4 ± 9.8 | 19.6 ± 4.8 | 15.93 ± 0.09 | 1.96 ± 0.08 | 20.2 ± 7.9 | 12.86 ± 0.84 | 8.6 ± 3.3 |
| He I λ4471 ....... | 51.8 ± 6.3 | ... | ... | ... | 65.8 ± 6.2 | 12.96 ± 0.18 | 6.72 ± 0.57 |
| | 59.5 ± 6.4 | 20.0 | 16.0 | 2.01 | 65.3 ± 7.7 | 13.10 ± 0.16 | 6.11 ± 0.45 |
| He II λ4686[b] ..... | 14.1 ± 6.9 | ... | ... | ... | 54.4 ± 6.6 | 12.95 ± 0.22 | 6.25 ± 0.70 |
| | 21.4 ± 4.8 | 17.9 ± 6.5 | 15.73 ± 0.11 | 2.02 ± 0.12 | 56.0 ± 5.1 | 13.14 ± 0.13 | 5.67 ± 0.38 |

[a] Cross-correlation velocities of Balmer lines.

[b] Cross-correlation velocities of rebinned He II λ4686 line.

note that the $K$ velocities are relatively low, although the helium lines have $K$ velocities consistently larger than the Balmer lines. While the poorer quality data of 1985 January 16 only spanned ~2.5 hr, and were interrupted, they nevertheless show the 2.1 hr period (Fig. 3*d*).

In the 10 rebinned spectra, a sharp emission feature, which we identify as Mg II λ4481, is seen with varying intensity. The line appears narrower than all the other lines. We note that the $\gamma$ velocity for the He I λ4471 line is 30–40 km s$^{-1}$ higher than for the Balmer lines and He II λ4686. A possible explanation is the presence of the Mg II λ4481 line in the red wing of He I λ4471, causing the centroid of the combined feature to be redshifted with respect to the uncontaminated line. An asymmetry in He I λ4471 has been attributed to this in the spectrum of SU UMa (Thorstensen, Wade, and Oke 1986). Mg II λ4481 emission is also often present in AM Her (Stockman *et al.* 1977; Greenstein *et al.* 1977), while it is seen in absorption in the nova-like variable RW Tri (Kaitchuck, Honeycutt, and Schlegel 1983).

### *d*) *Line Wings and the Broad Component*

In most CVs, the structure of the emission lines is of sufficient complexity to warrant a careful analysis of the velocity variations as a function of the position in the line where the velocity is determined, or weighted. Gaussian (or even Lorentzian) profile fitting is dominated by the lower velocity core, which is likely to include contributions from the outer accretion disk, the disk/accretion stream interface (i.e., the "hot-spot" or "bulge"), and other possible areas of enhanced emission in the outer disk regions. It is generally agreed that choosing a position to determine the velocity in the wings of the line profile results in a radial velocity curve more representative of the white dwarf's motion. This higher velocity material arises presumably in the inner parts of the disk where the Keplerian velocities dominate and is subsequently free of the contamination by, for example, a hot-spot or similar perturbation (e.g., Horne, Wade, and Szkody 1986).

We have used an algorithm which is in essence the double Gaussian convolution scheme used by Schneider and Young (1980), Shafter (1983, 1985), Shafter, Szkody, and Thorstensen (1986), and Horne, Wade, and Szkody (1986). The method determines the velocity from the line wings and remains insensitive to core velocity variations. A mask consisting of two Gaussian passbands, one in the red wing and one in the blue wing, separated by $a$(Å) is stepped through the profile until equal amounts of convolved flux appear in each passband. The midposition of the Gaussians, or "filters," defines the line center. The width of these filters is chosen so that enough flux is present for a meaningful measurement, while trying to minimize the contribution from the core-dominated part of the profile.

Since the signal-to-noise ratio is diminished in the line wings, we found it prudent to use this technique, referred to here as the Gaussian filter method, on the rebinned data. The Balmer lines Hδ, Hγ, and Hβ were measured using Gaussian separations from 10 to 50 Å in steps of 10 Å (i.e., at wing positions ranging from ~300 to ~1500 km s$^{-1}$ from the line center for Hβ). The radial velocities were fitted as in § III*b*, and the variation of the parameters $\gamma$, $K$, and $T_0$ were investigated as a function of separation i.e., position in the line wing.

The core-dominated regions of the line follow the smooth ~6.5 hr orbital velocity variation. As we move further into the line wings, the velocities seem to become increasingly dominated by the ~2.1 hr spin modulation. The velocities as a whole also become somewhat more negative (i.e., the $\gamma$ velocity decreases), and the spin-modulated velocity amplitude increases. At positions furthest from line center, the definition of where the wings begin and the continuum ends becomes a problem, and the velocities are increasingly erratic, owing to poor statistics. In Figure 4, we show the radial velocity results for Hλ, the highest signal-to-noise line.

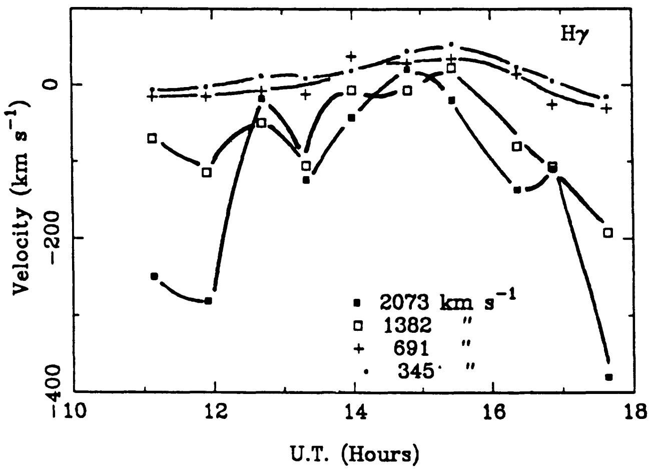

FIG. 4.—Radial velocity variations of the Hγ line on 1985 January 17, as determined by the Gaussian filter method (see text), at four positions in the line wings: 345, 691, 1382, and 2073 km s$^{-1}$ from line center.

## III. PHOTOMETRY

### *a) Observations*

A log of photometric observations conducted on H0534−581 is included in Table 1. Several runs of photometric observations were conducted on H0534−581 from 1984 to 1986 February. Both *UBVRI* photometry and high–time resolution (~200 ms) monitoring observations were carried out on the SSO 1.0 m and 2.3 m telescopes.

Most of the *UBVRI* observations, conducted with the two channel chopping photometer (TCC) in 1984 October and November, were reported in Paper I. A description of the TCC is also given in Paper I. The observations conducted on 1985 November 11 were arranged to be simultaneous with *IUE* observations of H0534−581, which are to be presented elsewhere (Bonnet-Bidaud *et al.* 1990).

Continuous high–time resolution *B*-band photometric monitoring was carried out during two runs in 1985 January and 1986 February. The instrumental setup was identical to that discussed in Paper II for 1H0542−407.

### *b) Period Analysis of the Optical Photometry*

A time series analysis was undertaken of the *UBVRI* (TCC) and high-speed photometric data using a discrete Fourier transform (DFT) method (e.g., Deeming 1975) discussed in Paper II. This technique was applied in a consistent manner to both the individual and combined runs of photometry. Period searches were conducted in four intervals: 200–1000 s, 1000–3000 s, 3000–10,000 s, and 10,000–50,000 s. The results of these searches are given below, except for the first interval for which no persistent or strong periods were detected. The periodograms are shown in Figures 5, 6, and 8, together with the window functions (lower panels of each figure) which indicate the presence of pseudoperiodicities introduced by the unequal sampling of the data, and which help to indicate the reality of a particular period (e.g., Deeming 1975).

#### i) *The 1000 s to 3000 s Interval*

For the longest and most complete high-speed photometry run (1986 February 12, 14, and 15), we find the strongest period peaks occur at 2707 and 2796 s (Fig. 5), both being 1 day aliases of the other. These periods are also seen in the 1985 January photometry and the periodogram of the combined high-speed data set. Also present in the 1986 February photometry is a shorter period at 1993 s, or possibly its 1 day alias at 1948, 2040, and 2090 s.

We now turn to the *UBVRI* photometry (TCC data). For the data set consisting of the sum of all runs, the strongest periodicities are at 2550 s/2625 s and 1932 s/1980 s. The period pairs are aliases of each other and have similar power, with the most dominant depending upon the particular passband. These periods compare favorably to the previously reported periods (Paper I) of 1915 ± 40 s, 2550 ± 70 s, and 2540 ± 50 s, derived from an epoch-folding period-finding technique on the three individual nights of data in 1984 (October 24, November 17 and 18). A DFT analysis of the longest run of *UBVRI* photometry (1984 November) resulted in the detection of the strongest periods at 2625, 1938, and 1310 s, or their adjacent 1 day aliases (Fig. 6). The first and last of these periods may well be associated (i.e., the fundamental and first harmonic, respectively). We find that the common periods for all of the *UBVRI* data sets are, therefore, 2625 and 1938 s, and in Figure 7*a* and 7*b*, the *U*, *B*, *V*, and *R* light curves derived from folding the combined data at these two periods are plotted. Interestingly, it appears that the pulse fractions are basically independent of color. In Table 4, we list the ephemerides and semiamplitude pulse fractions of these light curves.

We conclude this section by stating that the common periods to *all* of our optical photometry (high-speed and

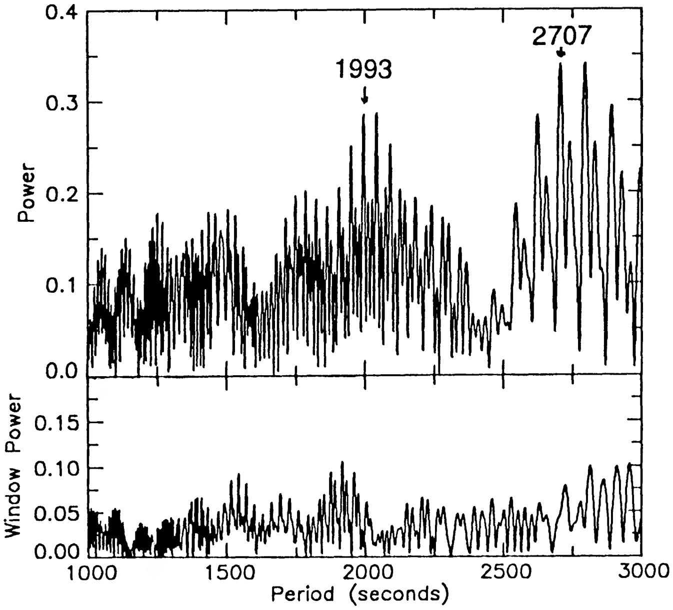

FIG. 5.—Discrete Fourier transform (DFT) periodogram in the interval 1000–3000 s of the high-speed *B*-band photometry obtained on 1986 February 12, 14, and 15. Lower panels are the spectral window functions, which indicate spurious periods resulting from effects of unequal data sampling.

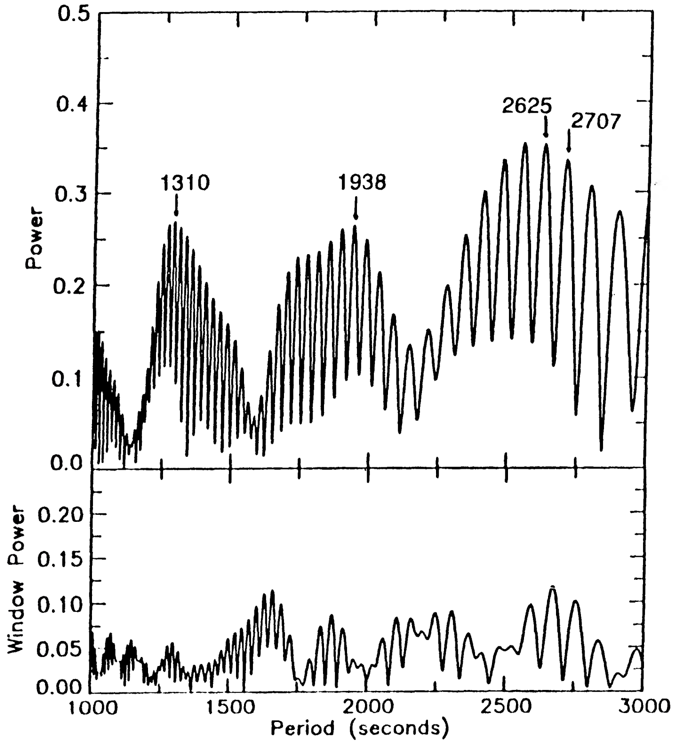

FIG. 6.—Discrete Fourier transform (DFT) periodogram, in the interval 1000–3000 s, of the *UBVRI* photometry obtained on 1984 November 17 and 18. Lower panels are the spectral window functions.

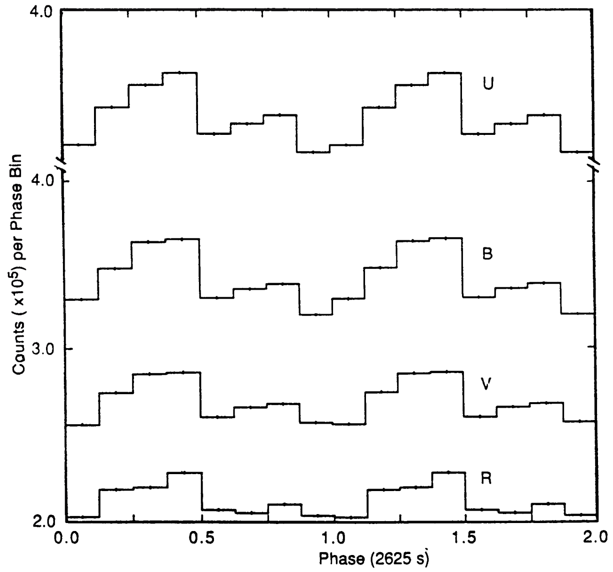

FIG. 7*a*

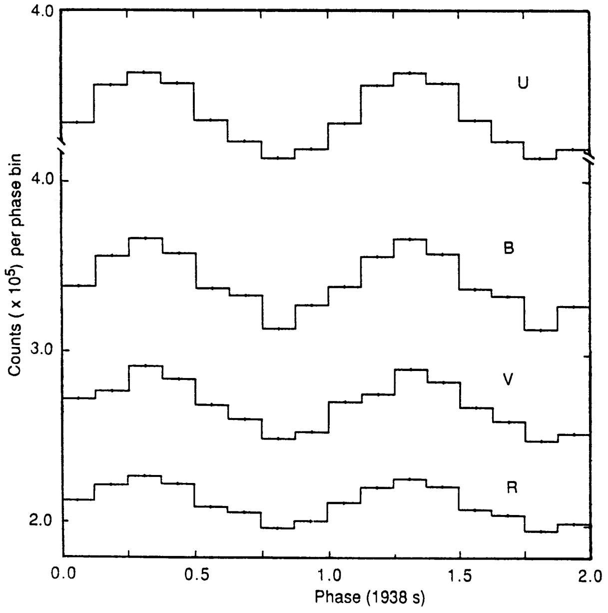

FIG. 7*b*

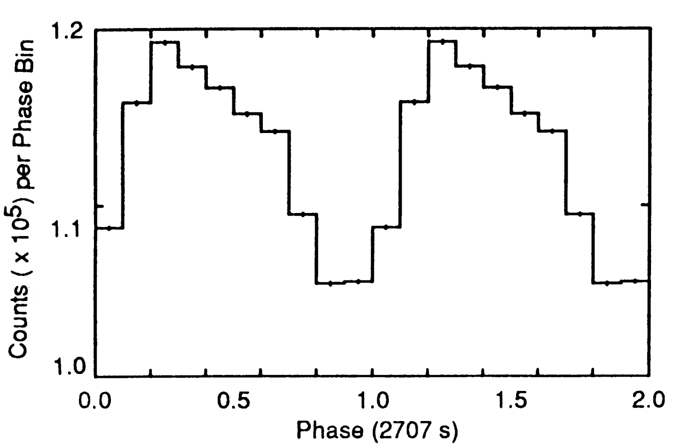

FIG. 7*c*

FIG. 7.—Optical light curves of H0534−581 obtained by folding the data at the respective dominant periods: (*a*) *UBVR* photometry with 2625 s period (*a*) and 1938 s period (*b*), and high-speed *B*-band photometry folded at 2707 s.

*UBVRI*) are 2707 s, and, possibly, 1938 s. In Figure 7*c*, the high-speed *B*-band light curve, derived from folding the entire high-speed data set at 2707 s, is presented. Its ephemeris is also included in Table 4. Finally, we note that the *UBVRI* data also folded at 2707 s (the alias of 2625 s) results in light curves virtually identical to those produced using the latter period.

### ii) *The 3000–10,000* s *Interval*

The spectroscopically determined period of 2.1 ± 0.1 hr (7560 ± 30 s) corresponds to no significant period peak in any of the periodograms of either the high speed or *UBVRI* data and is therefore not considered to be particularly significant when compared to nearby period peaks. Before we identified the likely origin of the 7560 s (2.1 hr) spectroscopic period as the white dwarf spin period, we pursued the hypothesis that the spin period was the ~1938 s period, or an alias, while the 2707 s period was the orbital sideband period at $P_s = (1/P_{\rm spin} - 1/P_{\rm orb})^{-1}$. This argument implied an orbital period of ~6800 s, or ~7400 s if we adopted a 1980 s spin period. We have found no evidence for the presence of any of these periods, or any close by, in any of our optical photometry. Our conclusion is that no optical modulations is present at the 2.1 hr spectroscopic period, and that neither is there any evidence of an orbital period in the range 1.9–2.1 hr.

### iii) *The 10,000–50,000 s Interval*

Finally the interval 10,000 s–50,000 s, spanning the second spectroscopic period of 6.5 ± 1 hr (23,400 ± 3600 s), was searched for periodicities. We found that the strongest period in the combined high-speed data set was at 23,520 s (6.53 hr), and the corresponding periodogram is shown is Figure 8*a*. This peak is also present in the 1986 February photometry, although the strongest period peak in this data set occurs at 11,864 s, close to the first harmonic at 23,520 s. These two periods, and their aliases, account for virtually all of the period peaks seen in the DFT (Fig. 8*b*). The 23,520 s period is close to the maximum of the very broad peak observed in the periodogram for the 1985 January data.

Turning now to the *UBVRI* photometry, we show in Figure 8*c* the DFT periodogram for the entire data set. The strongest period occurs at ~20,090 s (~5.6 hr), which is also seen as a

TABLE 4

ELEMENTS OF THE OPTICAL AND X-RAY LIGHT CURVES

| Light curve | Period (s) | $T_{\rm max}$ (J.D. −2,440,000) | Pulse Fraction |
|---|---|---|---|
| *B* (high-speed) ...... | 2705<br>23520 | 6089.007<br>6089.093 | 12%<br>20 |
| *U*, *B*, *V*, and *R* ......<br>(TCC) .............. | 2625<br>1938 | 5998.159<br>5998.152 | 6<br>8 |
| LE .................. | 7560 | 6023.012 | 36 |
| ME .................. | 7560 | 6023.012 | 17 |

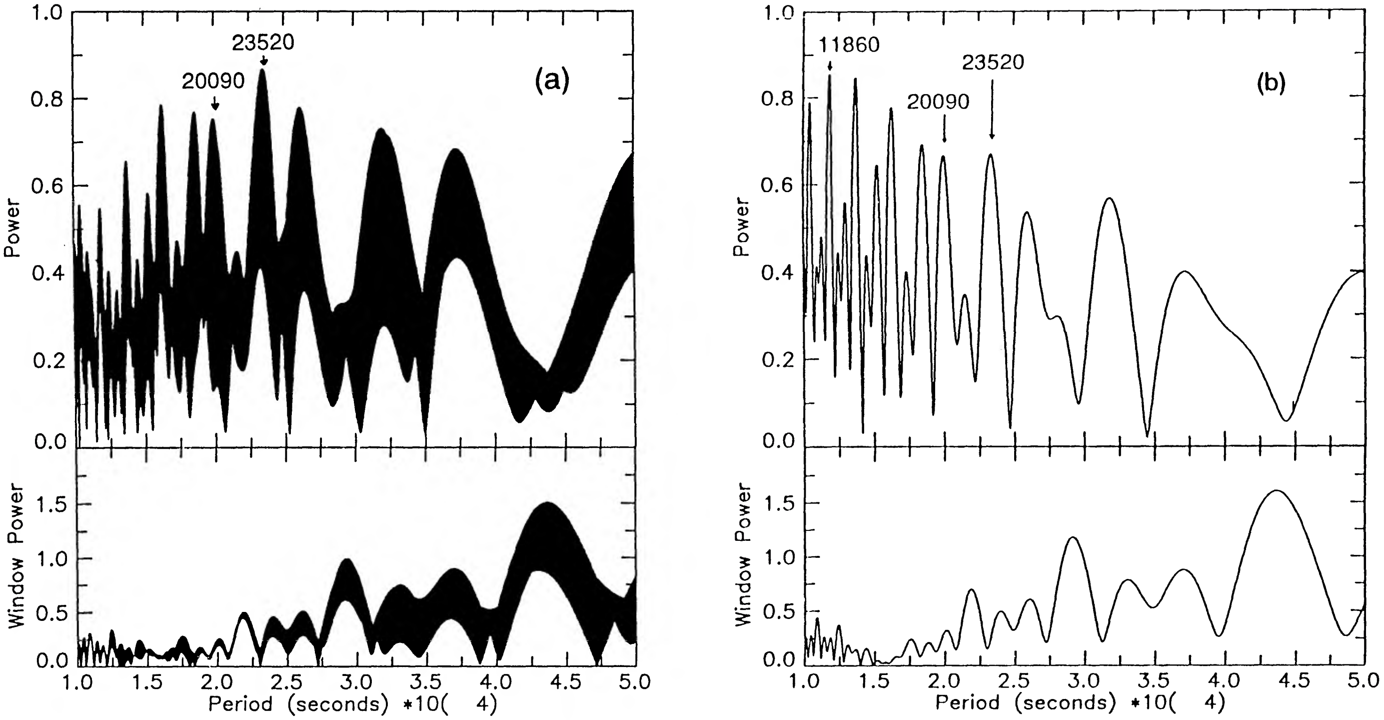

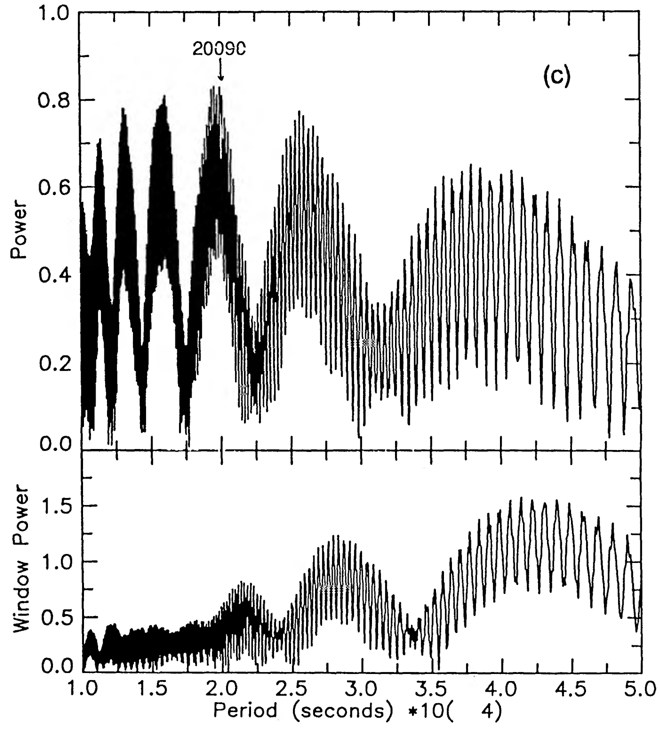

FIG. 8.—Discrete Fourier transform (DFT) periodograms in the interval 10,000–50,000 s for the following photometric data sets: (*a*) the entire high-speed *B*-band photometry (1985 January 23 and 24, and 1986 February 12, 14, and 15), (*b*) the latter (1986) data, (*c*) the entire *UBVRI* photometry (1984 October 24, November 17 and 18, and 1985 November 11). Lower panels are the spectral window functions.

minor period peak in the high-speed periodogram. We can therefore identify two periods, 20,090 and 23,520 s, which are within the uncertainties of the longer, probable orbital, spectroscopic period. The possible presence of the first harmonic of the 23,520 s period, at 11,760 s, could be considered as evidence that the 23,520 s is the true period. Alternatively, we have the possibility that the observed 11,860 s period is the beat period between the observed orbital period (23,520 s) and a ~7880 s (~2.19 hr) spin period. While the latter is within the uncertainties of the spectroscopic result (2.1 ± 0.1 hr), the absence of either the orbital (23,520 s) or presumed sideband (11,860 s) periods in any of the *UBVRI* data makes this an unlikely proposition. However, the absence of common periods between the two data sets (i.e., high-speed and *UBVRI*) may just be a consequence of the poorer phase coverage of the *UBVRI* data, which only averages ~3.5 hr continuous coverage per night.

In Figure 9, we present the *B*-band light curve, which is produced from folding all of the high-speed photometry at the 23,520 s (6.53 hr) period. The quasi-sinusoidal variation has a semiamplitude pulse fraction of ~20%. In Table 4, the ephemerides of this light curve are given.

### *c*) *X-Ray Period Reanalysis*

The *EXOSAT* medium energy (ME: 2–6 keV), and lower energy (LE: 0.1–2 keV) data reported in Paper I were reanalyzed in the same manner as the optical data using the DFT code. Only for the search interval 3000 to 10,000 s was a common period of some significance found in *both* the LE and ME data. Periods at ~7330 and 7560 s (± ~270 s) were found for the ME and LE, respectively (Fig. 10*a* and 10*b*). These periods are self-consistent and coincide with the (7560 ± 360 s) 2.1 ± 0.1 hr spectroscopic, probable spin, period.

Our DFT analysis confirms the presence of the previously reported periods in the ME data (Paper I) derived from epoch

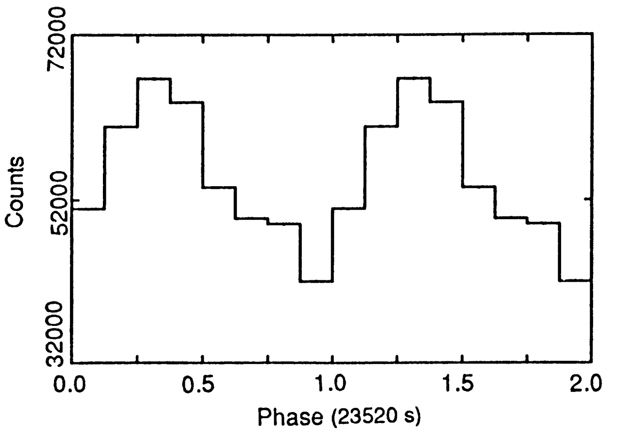

FIG. 9.—High-speed *B*-band orbital light curve derived from folding the data at the 23,520 s (6.53 hr) period.

folding. For the LE data, we find agreement with two periods previously reported in Paper I; the strongest at ~7500 s and the other at 5660 s.

We conclude, therefore, that the spin period of the white dwarf is detected in both the low- and medium-energy X-rays, and in Figure 11*a* and 11*b* we show the two light curves produced from folding the data at 2.1 hr. The ephemerides are given in Table 4. As in other intermediate polars, we note that the pulse fraction increases for lower energies, being $\sim 17 \pm 10\%$ for the 2–6 keV light curve, and $\sim 36^{+11}_{-16}$ for 0.1–2 keV.

### IV. ORBITAL PARAMETERS

As we have mentioned earlier, the Balmer line *K* velocities may suffer from perturbations arising from the hot-spot, disk nonuniformities, etc. If we accept that the He II velocity arises from the inner disk regions, or at least that this region *dominates* the emission, then it is safer to use the He II *K* velocity to derive the mass function. We have therefore adopted the He II value of $55 \pm 4$ km s$^{-1}$ and an orbital period of $6.5 \pm 1.0$ hr. Furthermore, we invoke the empirical mass-period relation of Patterson (1984) to derive a likely secondary mass of 0.6 $M_\odot$. The secondary mass function is hence

$$f(M_2) = \frac{P_{\rm orb} K_1^3}{2\pi G} = \frac{(M_2 \sin i)^3}{(M_1 + M_2)^2}$$
$$= 4.6 \pm 1.2 \times 10^{-3}\ M_\odot\ . \qquad (2)$$

The upper limit on $M_1$ of ~1.4 $M_\odot$ implies an upper limit on the orbital inclination of ~26°. In Table 5, we list the mass ratio ($q$), the separation of the stars ($a$), inclination ($i$), and several other parameters, which will be discussed in later sections, for a range of white dwarf mass 0.6–1.4 $M_\odot$. In Figure 12, we show the diagnostic mass-mass diagram which shows the combination of allowed masses of the component stars as a function of the orbital inclination. The uncertainties in both the period (~1 hr) and *K* velocity (~5 km s$^{-1}$) affect the placement of the constant inclination contours, and in Figure 13 we show the 20° inclination contour derived for the above value of $f(M_2)$ and its upper and lower limits.

While it seems certain that the orbital period must be the longer of the spectroscopic periods (i.e. 6.5 hr), we have for completeness investigated the possibility that the orbital period is actually the shorter 2.1 hr period. If this is the case, then the mass function for such a low *K* velocity (~20 km s$^{-1}$) is very small at ~7 × 10$^{-5}$ $M_\odot$. Furthermore, if we accept the empirical mass-period relationships (e.g., Faulkner 1971; Patterson 1984), then the secondary has a low mass of ~0.2 $M_\odot$ and implies that the inclination for the system is low, $\lesssim 16°$. If this latter scenario is indeed correct, then the longer spectroscopic period of 6.5 hr has to be explained. This period could be the spin period, in which case the white dwarf rotates slower than synchronism. However, no other X-ray periods have been

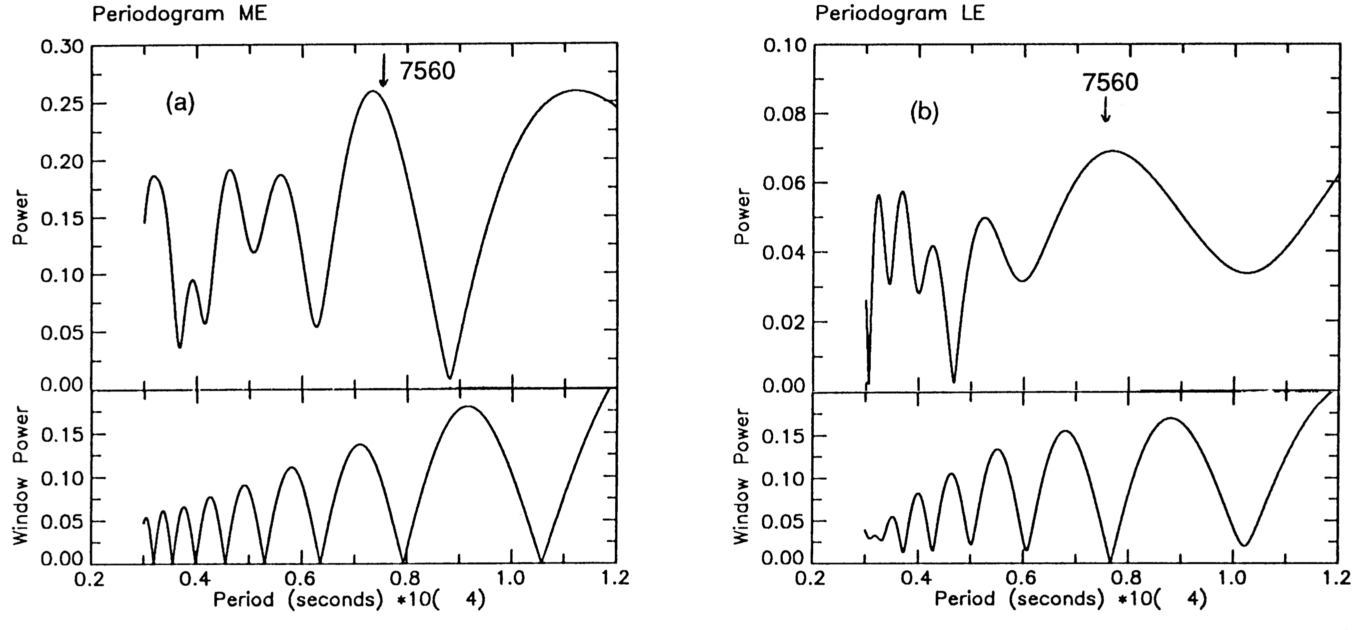

FIG. 10.—Discrete Fourier transform (DFT) periodograms in the interval 3000–12,000 s for the *EXOSAT* photometry (Paper I) in the energy ranges (*a*) 2–6 keV (ME) and (*b*) 0.1–2 keV (LE). The 2.1 hr (7560 s) spectroscopic period, identified as the likely spin period, is marked with an arrow. Lower panels are the spectral window functions.

TABLE 5

H0534−581 Binary Model Parameters

| $M_1$ ($M_\odot$) | $R_1$[a] (km) | $i$ (°) | $q$ | $a$ (km) | $r_c$ (km) | $r_c$ ($R_1$) | $r_J$ (km) | $\mu_{33}$ (g cm$^3$) | $B$ (MG) |
|---|---|---|---|---|---|---|---|---|---|
| 1.4...... | 1500 | 26 | 0.43 | $1.55 \times 10^6$ | $4.1 \times 10^4$ | 27 | $2.6 \times 10^5$ | 0.29 | 85 |
| 1.2...... | 3850 | 24 | 0.50 | $1.49 \times 10^6$ | $4.4 \times 10^4$ | 11 | $2.4 \times 10^5$ | 0.36 | 6.3 |
| 1.0...... | 5500 | 22 | 0.60 | $1.44 \times 10^6$ | $4.8 \times 10^4$ | 9 | $2.2 \times 10^5$ | 0.44 | 2.6 |
| 0.8...... | 6300 | 20 | 0.75 | $1.37 \times 10^6$ | $5.2 \times 10^4$ | 8 | $1.9 \times 10^5$ | 0.59 | 2.4 |
| 0.6...... | 9600 | 18 | 1.00 | $1.30 \times 10^6$ | $5.8 \times 10^4$ | 6 | $1.7 \times 10^5$ | 0.90 | 1.0 |

[a] Derived from Nauenberg's 1972 mass-radius relation.

detected, including near 6.5 hr. It is therefore hard to see how an X-ray periodicity could be detected at the orbital period (2.1 hr), but not at a period identifiable with the spin period. We conclude that the evidence points to a conventional identification of the shorter spectroscopic period (2.1 hr) with the spin period of the white dwarf. This is supported by the observed X-ray variation at this period.

## V. SPIN VARIATION OF THE EMISSION LINES

After establishing the likely spin period of the white dwarf as ~2.1 hr, we binned the entire spectral data for 1985 January 17 into eight equally spaced phase bins over the 2.1 hr period. Each spectrum was corrected for the orbital motion using the radial velocity curve for He II λ4686, considered to best represent the white dwarf motion (§ IV). Line profiles were redetermined by the double Gaussian fitting routine, and the parameter variations for the Hγ and Hβ lines are shown in Figure 14. The quasi-sinusoidal variation in all the line parameters over the spin period can be clearly seen. This behavior is reminiscent of 1H0542−407 (Paper II); in particular, we note that both the radial velocity and the line width vary in phase. Variations of this nature are also observed in the AM Her systems. Stockman *et al.* (1983) and Schmidt, Stockman, and

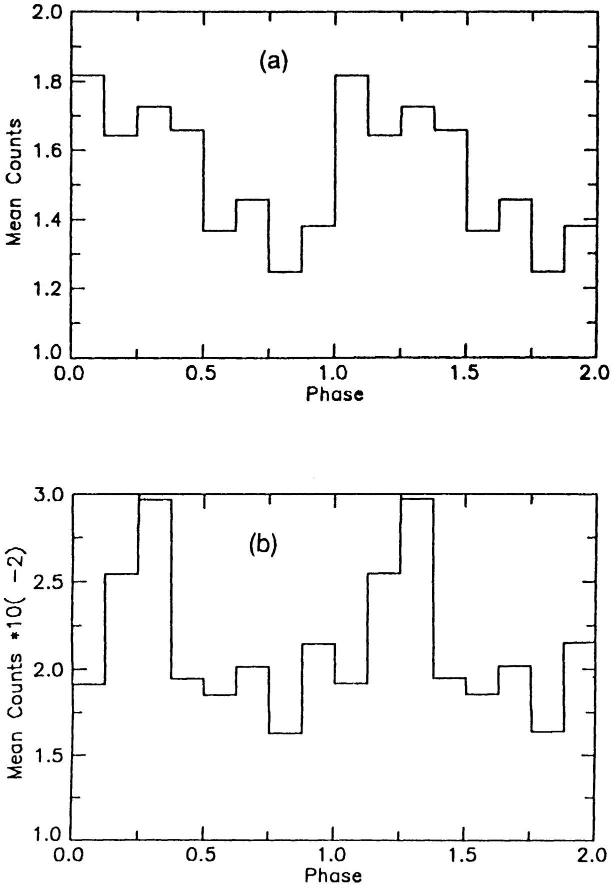

Fig. 11.—*EXOSAT* light curves obtained from folding the (*a*) 2–6 keV (ME) and (*b*) 0.1–2 keV (LE) data at the 2.1 hr (7560 s) period.

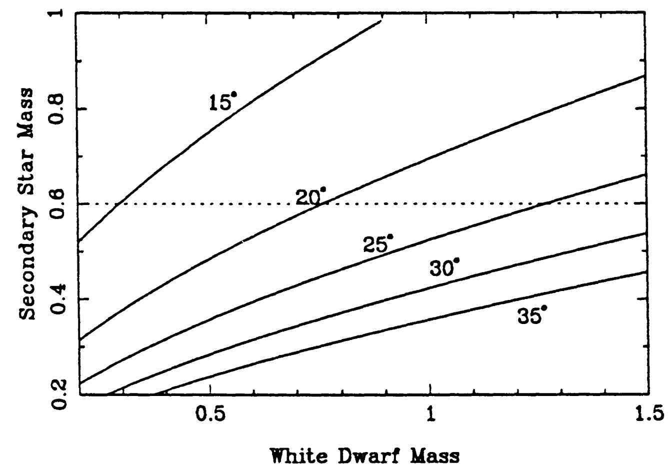

Fig. 12.—Diagnostic white dwarf mass–secondary mass diagram for H0534−581 assuming an orbital period of 6.5 hr and $K_{\rm wd}$ velocity ($=K_1$) of 55 km s$^{-1}$. Dotted line is the mass estimate of the secondary star based on Patterson's (1984) empirical mass-period relation. Solid curves are the constant inclination solutions. Mass units are in solar masses.

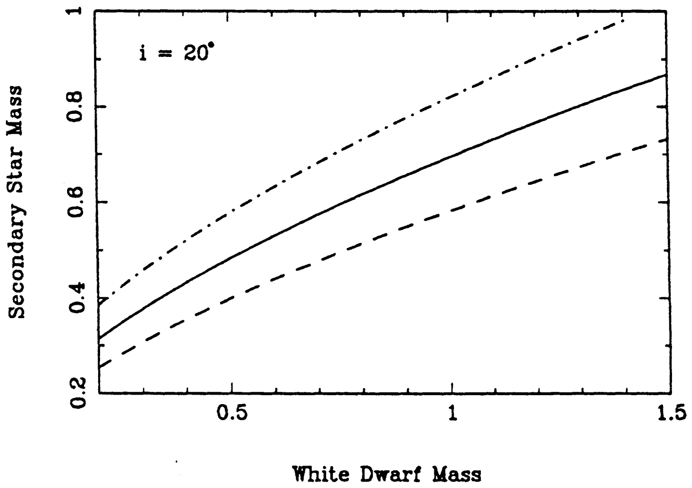

Fig. 13.—Same diagram as for Fig. 12, showing the effect of uncertainties on the position of the $i = 20°$ contour.

Grandi (1983) found in the case of CW1103+254 that the line FWHMs and velocities vary in unison over the rotation (=orbital) period. These authors have interpreted this behavior as a result of the rotation of an accretion funnel. They explain the observed phase lag between the velocity and FWHM curves as resulting from curvature in the accretion stream.

Velocity variations at the spin period of the white dwarf primary are becoming a commonly observed characteristic of the longer period DQ Her systems (intermediate polars). Such variations were reported by Penning (1985) in the four systems V1223 Sgr, AO Psc, FO Aqr, and BG CMi. Modulation of the emission-line parameters at the white dwarf spin period have been seen in other intermediate polars before; for instance, Shafter and Targon (1982) report spin-modulated line and continuum fluxes in FO Aqr.

We note in Figure 14 that the velocities of the narrow and broad Gaussian components of the two Balmer lines seem to be ~180° out of phase, as well as having significantly different $\gamma$ velocities. To investigate this further, we utilized the Gauss-

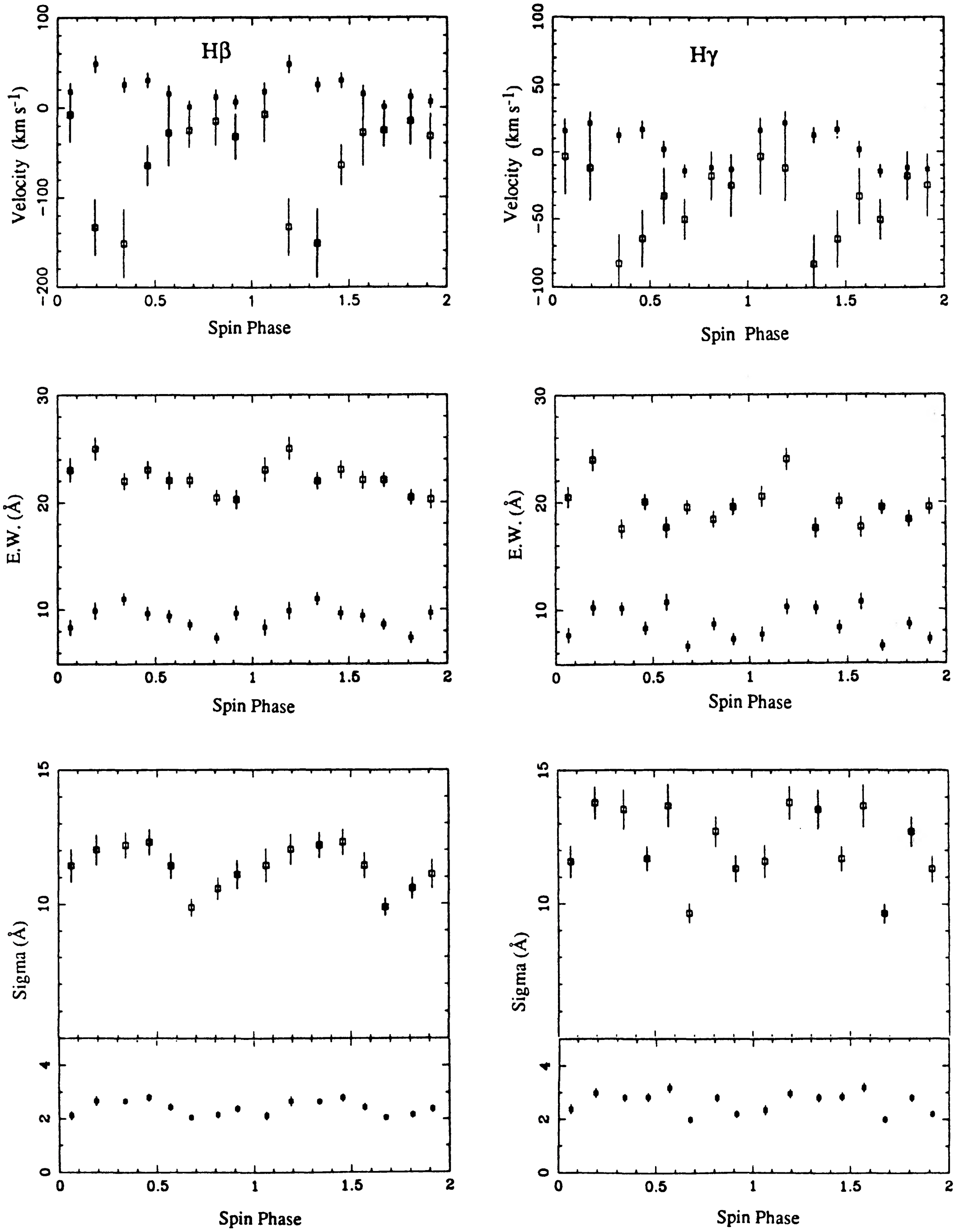

FIG. 14.—Radial velocity, equivalent width, and sigma variations of the narrow (■) and wide (□) Gaussian components for the lines H$\beta$ and H$\gamma$ on 1985 January 17.

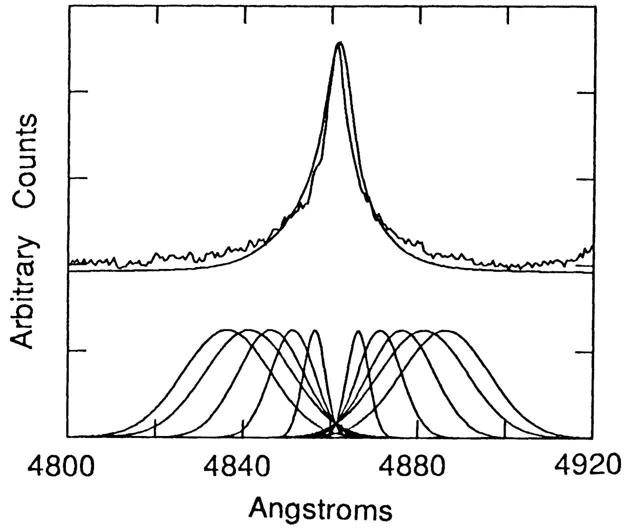

FIG. 15.—*Top*: mean observed H$\beta$ profile (*jagged line*), together with the simulated profile (see text). *Bottom*: passbands used in the Gaussian filter method (see text) to determine radial velocities in the line wings. Separations of the blue and red filters are 50, 40, 30, 20, and 10 Å, while the corresponding widths (sigmas) are 10, 10, 7.5, 5, and 2.5 Å.

ian filter method (§ III*c*) to measure the wing velocities and to see if there was a gradual or abrupt change in the radial velocity parameters as we moved from the narrow core of the line into the broad wings. The passband, or filter, separations were the same as used in § II*d*, while the sigmas of the Gaussians were 2.5, 5, 7.5, and 10 Å for separation of 10, 20, 30, and $\geq$40 Å. The filters and their positions near line center are shown in Figure 15, together with the mean H$\beta$ profile and a simulated profile which is discussed in the next section (§ VI*d*).

In Figure 16, the radial velocity curves derived at the various positions in the line profile are presented. It is clear that as we move from the core-dominated region into the wings, the radial velocity parameters $\gamma$, $K$, and $T_0$ vary monotonically as a function of position from line center, as can be seen in Figure 17. This behavior and possible explanations are discussed in the next section.

## VI. ORIGIN OF THE SPIN MODULATION

In this section, we attempt to explain the observed spin modulation of the velocities in terms of two possible models: (*a*) the illuminated accretion disk spot model of Penning (1985), and (*b*) the magnetospheric disruption model which we devel-

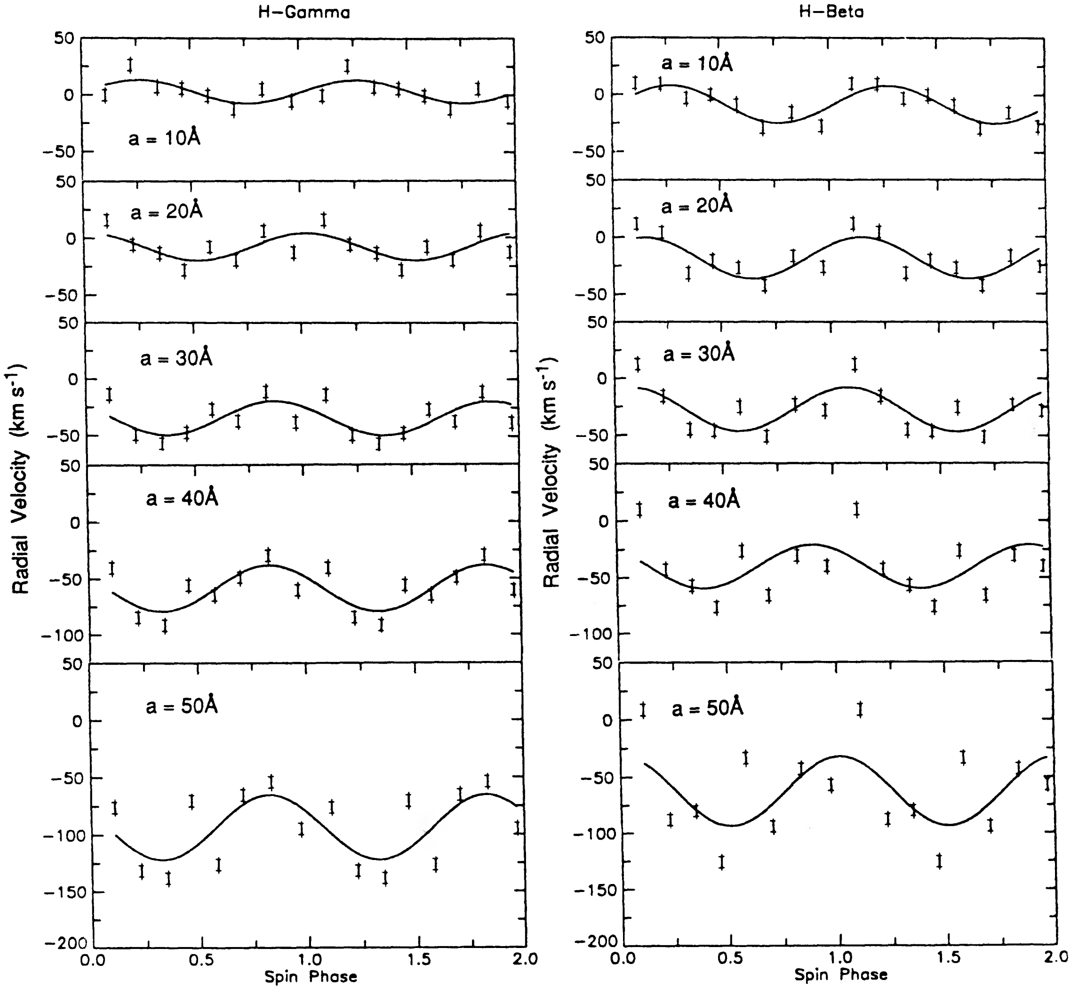

FIG. 16.—Variations in the radial velocity curves for H$\gamma$ and H$\beta$, derived from the Gaussian filter method (see text), as a function of the filter (passband) separation *a*.

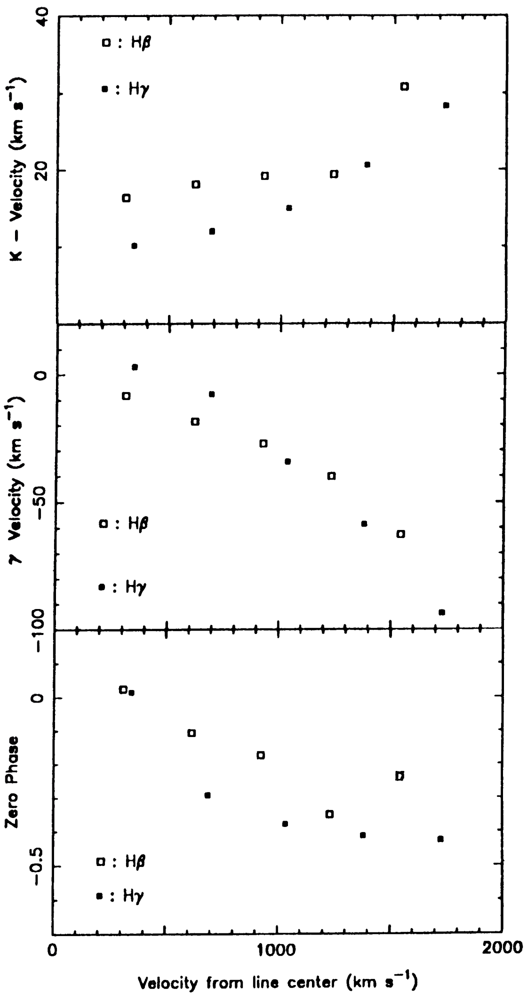

FIG. 17.—The dependence of the radial velocity curve parameters ($K$ velocity, $\gamma$ velocity, and zero phase) as a function of position from line center where the velocity is determined. Radial velocities were determined using the wing sensitive Gaussian filter method (see text).

oped for 1H0542−407 in Paper II. We then address the behavior of the core and wing radial velocity curves.

### *a*) *Illuminated Spot Model*

Penning (1985) has attempted to explain the spin velocity "excursions" as arising from a spot on the accretion disk illuminated by a beam of X-rays from the white dwarf. At any one time, the reprocessed optical emission from the spot enhances the specific intensity of the accretion disk over a velocity space representative of the mean projected Keplerian velocity of the spot. As the white dwarf rotates, the beam moves in azimuth, illuminating different regions of the disk. At a particular rotation phase, the velocity of this spot is simply the mean Keplerian velocity of the material moving through it.

The distance of the illuminated spot from the primary is given approximately as

$$R_{\text{spot}} \sim \frac{GM_1 \sin^2 i}{K_2^2} . \tag{3}$$

Again we find, as for 1H0542−407, that the Penning model requires the illuminated spot to be a distance greater than the separation of the stars. Even increasing the spot's size does not help a great deal in decreasing this distance. The increased azimuthal extent, which might help lower the mean velocity of spot material, is offset by the inclusion of faster moving, brighter material from closer in to the white dwarf.

### *b*) *Magnetospheric Disruption Model*

We have shown in Paper II that in the case of 1H0542−407, and probably also for V1223 Sgr and BG CMi, that an alternative explanation for the spin velocity modulation, which we proposed in that paper, is the corotation of accreting gas trapped in the white dwarf's magnetosphere. At some distance from the white dwarf, the magnetic pressures overwhelm the Keplerian motion of the disk material, forcing it so slow down and corotate with the white dwarf/magnetosphere. This distance is approximated by the magnetospheric radius.

The disruption of the accretion disk will not be a sudden transition at the minimum disk radius, $R_{\text{in}}$; rather, it will occur over a region of the disk $\Delta r$, where $\Delta r \sim R_{\text{in}}/3 \sim \nabla B/B$ (e.g., Rosen, Mason, and Córdova 1988), due to the $r^{-3}$ nature of the magnetic dipole forces. Magnetic field lines intersecting the disk in this region will slow down the rotating material and feed it along the field lines to the polar regions. For a tilted dipole model, the area of the white dwarf surface that contains the footprints of these field lines is a thin arc-shaped region of approximately constant magnetic latitude. Such regions of extended longitude, but having low fractional area $f$, are able to explain the morphology and energy dependence of the X-ray light curves in the intermediate polars (Rosen, Mason, and Córdova 1988; Paper II).

In the case of the magnetospheric disruption model, the distance of the corotating material responsible for the spin-modulated emission is given as

$$R_c \sim \frac{K_2 P_{\text{spin}}}{2\pi \sin i} , \tag{4}$$

and these distances are also given in Table 5. We note that the addition of an emission component whose velocity is constant over the spin period (for example, the disk) will tend to decrease the observed $K_2$ velocity amplitude, resulting in a systematically smaller $R_c$. However, our profile simulations (§ VII*d*) indicate that at worst, this would result in underestimation by a factor of $\sim 2$. The overall result is that if the spin-modulated velocity variations arise in a region corotating with the magnetosphere, then its distance from the white dwarf is between $\sim 4$ and $7 \times 10^4$ km, or $\sim 30$ to $\sim 5$ white dwarf radii, with an error of $\sim 50\%$, for the limits 1.4 and 0.4 $M_\odot$.

### *c*) *Accretion within the Magnetosphere*

Since the likely mechanism for a spin-induced velocity variation is corotation with the white dwarf, or rather its magnetosphere, then it is reasonable to invoke a rotating accretion funnel/stream as in the AM Her systems. One of the best studied DQ Her systems in which the spin modulation of the emission lines has been addressed is EX Hya (Kaitchuck *et al.* 1987; Hellier *et al.* 1987). The former authors have developed a model to explain the line strength and width variations at the spin period in which accretion funnels over both magnetic poles are important sources of line emission. If the line emission is optically thick, then a peak in line intensity occurs when the line of sight is closest to the magnetic axis, where the funnel presents its greatest projected area. The line width is also at a maximum in this situation, because we observe material streaming in two opposing directions, onto both magnetic poles. Kaitchuck *et al.*'s (1987) model predicts that a spin-modulated radial velocity will result from the rotation of the accretion funnels. Furthermore, the model predicts that the velocity and line width will be 90° out of phase, because the projection along the line of sight of the velocity vectors of the rotating funnels will be near zero when the funnel axes are closest to the line of sight, at line width maximum. To date, there is no reported velocity variation for EX Hya at the 67 minute spin period (Kaitchuck *et al.* 1987), although Hellier *et al.* (1987) do report a spin variation in the ratio of the red peak to blue peak intensities of the double peaked profiles, which can be interpreted as a velocity effect.

Since there probably is a symmetric accretion disk in the intermediate polars, we expect accretion onto both magnetic poles, or rather the associated extended "auroral" zones (e.g., Hellier *et al.* 1987; Paper II). The low inclination of H0534−481 implies that one of the poles (i.e., the pole above the disk plane) dominates the observed variations. We can then interpret the ~180° phase lag in velocity between the narrower and broader components of the lines as a result of the rotation of both accretion funnels. The broader component may be associated with the funnel which we see more clearly above the disk plane, while the narrower and weaker component is associated with the funnel below the disk plane, which is partly obscured by the accretion disk and the body of the white dwarf. As the white dwarf rotates, the funnels precess around the spin axis, resulting in velocity variations. However, the variations of the line-equivalent widths and sigmas, *in phase* with the rotation velocity, is difficult to explain in this model (e.g., see Paper II). An alternative could be that the velocity variations arise from the changing magnitude of the projected infall velocity of material in the funnel.

We return now to the results of the wing velocities discussed in § III*d*. The smooth variation of the radial velocity curve parameters as we move further into the line wings suggests the following *alternative* explanation of the velocity variations. If we adopt the magnetospheric disruption of the inner disk regions, then at approximately the inner disk radius (which for the moment we assume is $\sim 10 R_1$ for a 1 $M_\odot$ white dwarf), the material is suddenly slowed from quasi-Keplerian rotation, at a velocity of ~1500 km $s^{-1}$, to the corotation velocity of the magnetosphere, at ~50 km $s^{-1}$. An oblique shock is produced in which the accreting gas may become highly ionized, similar to the shock proposed by Hameury, King, and Lasota (1986) for diskless accretion directly onto a magnetosphere. The immediate postshock gas would be highly turbulent and would result in a local emission-line profile with a considerable FWHM of the order $10^3$ km $s^{-1}$. The postshock gas will recombine, giving rise to emission lines of hydrogen and helium, with possibly strong He II λ4686. The strong fluid shear at the disruption boundary will result in Kelvin-Helmholtz instabilities (Hameury, King, and Lasota 1986), and the material will subsequently accrete onto the white dwarf along the magnetic field lines. Contrary to the polars, where the gas is threaded by the field lines at larger distances, the threading region in intermediate polars is much closer to the white dwarf. In the former, the gas accretes at ~free-fall velocities (e.g., Wickramasinghe 1988), while for the intermediate polars, the threaded material accretes magnetohydrodynamically along the field lines at velocities considerably less than free fall. Hence, we do not see the large infall velocities in the emission lines at $10^3$–$10^4$ km $s^{-1}$, which are commonly observed in the polars. Also, at a distance of a few white dwarf radii, the gas becomes completely ionized, and we therefore do not see lines from this region at all.

The velocity of the partially ionized postshock gas is dominated by the random turbulent velocities. However, the rotation of the magnetosphere will introduce a periodic velocity shift. As the gas moves radially inward, the velocities become more ordered, with a decreased turbulent and corotation velocity and an increased infall velocity.

If this picture is indeed correct, then some observational predictions can be made. First, far out in the line wings, the emission-line profile is dominated by the motion of the immediate postshock material. Hence, this material will have the largest corotation velocity, and hence $K_{\rm spin}$. As we probe the profile in toward the core, the dominating source is somewhat closer to the white dwarf, and therefore has a smaller $K_{\rm spin}$. Also, the gas is beginning to move radially inward along the field lines, and hence the velocity vector of this gas is the sum of the corotation and infall velocity vectors. The increasing dominance of the infall velocity over the corotation velocity as the gas moves in leads to an expected gradual variation of the zero phase point of the radial velocity curves as we progress from the outer wings toward the core. Furthermore, the increase in the infall velocity experienced by the gas implies that the $\gamma$ velocity should also increase as we move in toward the core of the profile.

### *d) Model Simulations*

All of the above predictions are in fact borne out by our observations, as seen in Figures 16 and 17. The question remains, however, whether or not the observed variations are *uniquely* predicted by the above model. In an effort to address this, we have carried out an exercise based on line profile simulations. We assumed a null hypothesis that the spin-modulated emission-line profile was the sum of two Gaussian profiles, of varying amplitude and width, with their own radial velocity parameters $\gamma$ and $K$ (the period was assumed constant at $P_{\rm spin} = 2.1$ hr). The sigmas of the Gaussians were ~2 and 10 Å, respectively, the same as derived from the two-Gaussian profile fits to our data. An additional fixed Lorentzian profile of FWHM ~12 Å was added to account for the presence of an accretion disk. The simulated lines were calculated for the same eight phase bins as our observational data and were measured using the Gaussian filter method in exactly the same manner as our observations. By varying the amplitudes of the component profiles, plus $\gamma$ and $K$ velocities, we were able to reproduce velocity variations of similar behavior to our observations. Our choice of amplitudes was constrained such that the sum of the three component profiles (two Gaussians, one Lorentzian) approximated the observed profile. The simulated profile is included in Figure 15 with the observed mean H$\beta$ line. As the amplitude of the constant disk component was increased relative to the two comoving Gaussians, their $K$ velocities had to be increased so that the amplitudes of the radial velocity curves mimicked those of the real data. The $\gamma$ velocities for the narrow and broad components also had to become more red and blueshifted, respectively, for the same reason. While we could simulate the same $K$ and $\gamma$ velocity behavior as observed in Figure 16, the zero phase variation of the simulations never showed the gradual change seen in our data. There was always a more sudden jump in phase for the simulations from the core measurement at ~300 km $s^{-1}$ from

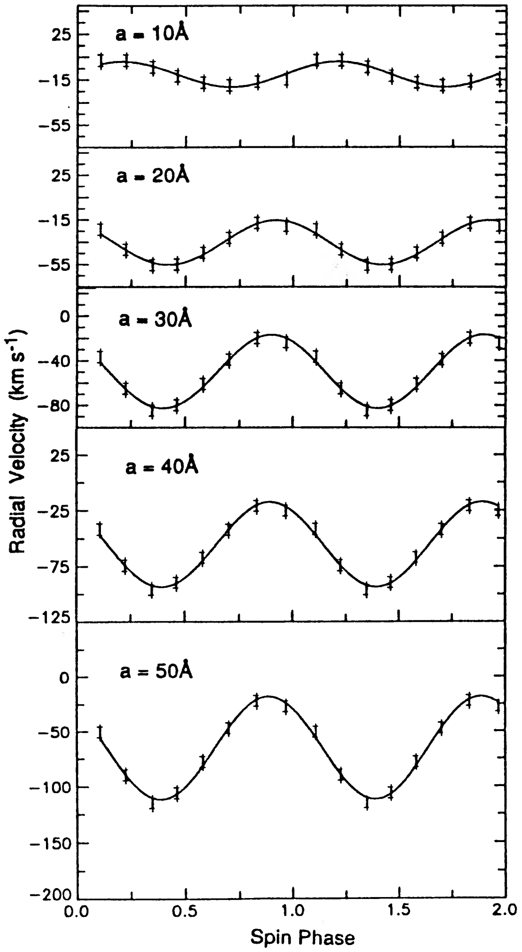

FIG. 18.—Variations of the radial velocity curves, derived using the Gaussian filter method, as a function of filter separation, *a*, for the two-component model simulation (see text).

line center to the start of the wings at ~600 km s$^{-1}$ from line center. While the scatter in the data becomes significant further out in the wings (from about 1200 km s$^{-1}$), the gradual shift in zero phase is even more compelling when we consider both the H$\beta$ and H$\gamma$ data together, as in Fig 17. The radial velocity curve simulations are shown in Figure 18.

Our conclusion is that while the two-component Gaussian model for the spin modulation of the emission lines can explain the gross features of the radial velocity curve variations, it cannot do so *uniquely*. It is equally possible that the profile consists of many Gaussians, or pseudo-Gaussians, all with smoothly varying $K$ and $\gamma$ velocities, as would be expected in the flow model discussed above.

## VII. DISCUSSION

### *a) A Diskless System?*

Wickramasinghe, Stobie, and Bessell (1982) argue that the nondetection of a spin-modulated line intensity implies that the accretion column/funnel contributes less than 15% of the total emission-line intensity. The remainder is contributed by the accretion disk. Conversely, we argue that for such a clear spin modulation of all the emission-line parameters (velocity, width, and intensity; see Figs. 3 and 16) to be seen requires that the region responsible for this component of the emission, which we identify as the magnetosphere, must contribute at least 15% and probably more of the line flux.

We ask now whether an accretion disk need be present at all in H0534−581. We invoke the models of King, Frank, and Ritter (1985) and Hameury, King, and Lasota (1986), who consider that accretion occurs directly from the secondary star onto the magnetosphere without the formation of an accretion disk. They maintain that the magnetosphere is large enough to prevent disk formation or to disrupt an existing disk. This model has been used by McHardy *et al.* (1987) in the case of the intermediate polar BG CMi (3A0729+103). They are able to explain the observed orbital modulation of the X-rays by invoking X-ray emission produced in the shock at the magnetosphere/accretion stream interface.

Lamb and Melia (1987) have shown that for an accretion disk to be present in an intermediate polar, the radius of the magnetosphere cannot exceed a certain limit. They define this limit to be the radius of the circularized accretion stream, or ring, defined as $\omega_{\max} \approx 0.09\text{–}0.16 R_{L1}$ (Lubow and Shu 1975). Alternatively, Shafter (1983) derives the following expression for the radius of an inviscid disk, under the assumption that the angular momentum of the transferred material is conserved:

$$r_J = a(1 + q)(0.5 - 0.227 \log q)^4 \, . \tag{5}$$

The magnetospheric radius for disk accretion is given by King, Frank, and Ritter (1985) as

$$r_\mu = 2.7 \times 10^{10} \mu_{33}^{4/7} \dot{M}_{16}^{-2/7} M_1^{-1/7} \phi \text{ cm} \, , \tag{6}$$

where $\mu_{33}$ is the magnetic moment in units of $10^{33}$ G cm$^3$, $M_1$ is the mass of the white dwarf in solar masses, and $\dot{M}_{16}$ is the mass transfer rate in units of $10^{16}$ g s$^{-1}$. The parameter $\phi$ depends upon the accretion geometry, being ~0.37 for diskless accretion (e.g., as in a polar). An estimate for $\dot{M}_{16}$ is obtained using Figure 3 of Lamb and Melia (1987), which is based on the magnetic braking theory of Rappaport, Verbunt, and Joss (1983). We obtain mass transfer rates of $4.5^{+1.6}_{-1.5}$, $7.2^{+3.8}_{-2.3}$, and $11^{+10}_{-4} \times 10^{16}$ g s$^{-1}$ for white dwarf masses of 1.4, 1.0, and 0.8 $M_\odot$.

All of these values are smaller than those obtained with either of Patterson's (1984) relations (empirical or theoretical), or Verbunt and Zwaan's (1981), and we therefore consider the above estimates to be conservative.

By equating the two radii $r_J$ and $r_\mu$, we are able to derive a lower limit to the magnetic moment, $\mu_{33}$, of between ~13 and 10 for masses 1.4–0.6 $M_\odot$. The implied surface field strengths are greater than 40 MG for masses $>0.8$ $M_\odot$, dropping to ~11 MG for $M_1 = 0.6$ $M_\odot$. Even if we take the conservative option of using $\omega_{\max}$ in the place of $r_J$, we still arrive at a rather high value for $\mu_{33}$ of 2–3. This, in turn, implies surface fields of greater than 10 MG for $M_1 > 1$ $M_\odot$. All these field strengths are larger than the estimates determined by Lamb and Patterson (1983) for other intermediate polars, based on spin period changes. Thus, we find that the criterion for the absence of a disk requires magnetic field values more in the regime of the polars than of the intermediate polars. We consider, therefore, the absence of a disk in such a long-period system to be unlikely, which is consistent with the lack of observational evidence to the contrary. This conclusion coincides with the view of Lamb and Melia (1987), who maintain that the magnetic moments of the intermediate polars are 1–2 orders of magnitude less than for the polars.

### *b) Estimate of Field Strength and Disk Size*

If we accept that the magnetospheric radius is approximately equal to the radius of the emission region responsible for the spin-modulated velocities ($R_c$; § VI*b*), then we can estimate $\mu_{33}$ and hence, $B$ following the same procedure above. We substitute a new value for $\phi$ of 0.5 in equation (6) for accretion via an accretion disk (King 1985). The range of $R_c$ of 4–6 × $10^4$ km (see Table 5), leads to values for $\mu_{33}$ ranging from ~0.3 to 0.6 for masses 1.4–0.6 $M_\odot$. The corresponding field strengths are ~6 MG for 1.2 $M_\odot$, or ~3 MG for a 1.0 $M_\odot$ white dwarf. These are certainly in the regime expected for the intermediate polars (Lamb and Melia 1987).

The fact that the magnetospheric radius, $r_\mu$, is approximately equal to the inner disk radius leads to a value for the latter of $\sim 9R_1$ for a 1 $M_\odot$ primary. If the outer radius of the disk is the maximum 90% of the mean Roche lobe, then the ratio of $R_{\rm out}/R_{\rm in}$ is ~11, within the uncertainties derived by Bonnet-Bidaud *et al.* (1990) from their disk model based on *IUE* observations.

### *c) The Short Persistent Optical Periods*

Because we have identified both spectroscopic periods with the spin and orbital velocities, we now discuss the apparently persistent short period(s) in the optical photometry, discussed in § III; namely, the 2707 s and possibly 1938 s periods.

The absence of a detectable velocity modulation at these shorter periods argues for the feature to be dominated by continuum emission. This could arise from optically thick blobs of material rotating in the disk at their Keplerian velocities. It is possible that these blobs are positioned near the disk's outer radius, although if we accept that the maximum outer disk radius is ~90% of the mean Roche lobe (e.g., Shafter, Szkody, and Thorstensen 1986), then it is more likely that such blobs are more centrally located. The observed coherency of the short period, not really expected in a model involving short-lived blobs, could be a consequence of the length of a single data sample (~5 hr), which is only ~6–7 times the period. In other words, the blobs survive this number of rotations before they disappear, resulting in the apparent coherency.

### *d) $F_x/F_{\rm opt}$: Comparison to Other X-Ray CVs*

We compare now the gross optical and X-ray properties of H0534−581 with other known hard X-ray–emitting cataclysmic variables. The majority of these CVs are nonmagnetic systems, where the X-rays are produced in a boundary layer between the accretion disk and the surface of the white dwarf (Shakura and Sunyaev 1973; Lynden-Bell and Pringle 1977). Patterson and Raymond (1985) have investigated the correlation between X-ray and optical parameters based upon the *Einstein Observatory* IPC observations of CVs (see Córdova and Mason 1983, 1984). In order to compare the properties of H0534−581 to other objects studied by Patterson and Raymond, we have converted the *EXOSAT* 2–10 keV flux of 2.9 × $10^{-11}$ ergs cm$^{-2}$ s$^{-1}$ (Paper I) to the *Einstein* IPC band 0.2–4 keV. This was achieved assuming an exponential spectrum with Gaunt factor. The resultant flux is $f$(0.2–4 keV) = 2.0 ± 0.2 × $10^{-11}$ ergs cm$^{-2}$ s$^{-1}$ for all allowed values of $N_{\rm H} < 5 \times 10^{20}$ H cm$^{-2}$. We have estimated the optical flux, $F_v$ ($\lambda\lambda$5000–6000), from our average flux-calibrated spectrum of 1985 January 18 to be 4.0 ± 0.2 × $10^{-12}$ ergs cm$^{-2}$ s$^{-1}$. The ratio of $F_x/F_v$ is therefore 5 ± 1, comparable to the highest amongst Patterson and Raymond's sample (similar to EX Hya), and in the range expected for magnetic variables (Córdova and Mason 1983). The other optical parameter which they employ is the H$\beta$ equivalent width (EW). Our results from the same spectrum (§ II*b* and Table 2) indicate a total mean H$\beta$ EW of 30.1 ± 0.3 Å. This quantity is shown to correlate well with $F_x/F_v$ by Patterson and Raymond; however, for H0534−581, $F_x/F_v$ is too high for the observed EW, although within the bounds of the scatter. It should be noted that uncertainties in $F_x/F_v$ arise from the non-simultaneity of the X-ray and spectroscopic observations.

### *e) Balmer Decrement*

We note that the hydrogen line ratios for H0534−581 are extreme compared to most cataclysmic variables (Echevarria 1988). The H$\gamma$/H$\beta$ and H$\delta$/H$\beta$ ratios are 1.29 and 1.73, respectively, for our average spectrum of 1985 January 17 (Table 2). This compares with the ratios 1.41 and 1.65 quoted in Paper I for the spectrum taken on 1984 February 8. Such large ratios are indicative of high disk temperatures, in excess of $10^5$ K (Drake and Ulrich 1980). Recent interpretation of *IUE* spectra of H0534−581 (Bonnet-Bidaud *et al.* 1990) has confirmed a central disk temperature of $\sim 10^5$ K.

### *f) The Spin-Orbital Period Correlation of Intermediate Polars*

Our final comment concerns the correlation between white dwarf spin period and orbital period in the long-period ($P_{\rm orb} > 3$ hr) DQ Her systems (intermediate polars). We have neglected the two fast rotators DQ Her and AE Aqr ($P_{\rm spin} = 71$ and 33 s, respectively), because their spin-down rates imply much weaker field strengths than the others (Lamb and Patterson 1983). Also not included is the long orbital period system GK Per, which is unusual in that it probably contains an evolved secondary. In Figure 19, we show a log-log plot of the periods of these systems, including H0534−581, which has both the longest spin and orbital period of the subgroup. It is also closest to the synchronism line $P_{\rm spin} = P_{\rm orb}$. As Barrett, O'Donoghue, and Warner (1988) have pointed out, the trend of

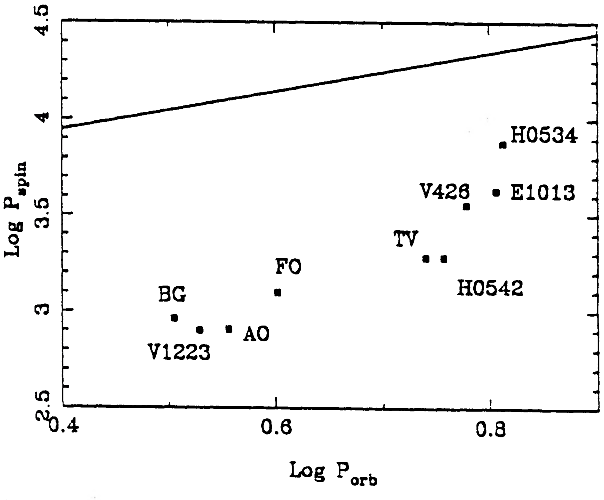

FIG. 19.—Orbital and spin period distribution (in units of log hours and log seconds, respectively) for the long-period DQ Herculis systems (intermediate polars), omitting DQ Her, AE Aqr, and GK Per (see text). The systems shown are (in order of increasing orbital period): BG CMi, V1223 Sgr, AO Psc, FO Aqr, TV Col, 1H0542−407, V426 Oph, E1013−477, and H0534−581. Abbreviations of the individual names are used. Sloping line at the top of the diagram is the synchronism line, $P_{\rm spin} = P_{\rm orb}$.

increasing $P_{\rm spin}$ with $P_{\rm orb}$ is contrary to the predictions of Chanmugam and Ray (1984), Hameury *et al.* (1987), and King, Frank and Ritter (1985), who consider that the magnetic moments, $\mu$, of DQ Her and AM Her systems are similar, and conserved during their evolution. In their scheme, a DQ Her system, evolving to a shorter orbital period through loss of angular momentum, would move along contours of constant $\mu$ in a direction generally to the upper left of Figure 19, *increasing* its spin period as the orbital period decreases. Although only dealing with a relatively small sample (9), with H0534−581 we confirm the trend of increasing spin period with orbital period.

## VIII. SUMMARY

We have identified two spectroscopic periods in H0534−581 at 2.1 and 6.5 hr, which we interpret as the white dwarf spin and orbital periods, respectively. A reanalysis of the *EXOSAT* light curves has resulted in the detection of the 2.1 hr spin period which exhibits the expected increased pulse fraction toward lower energies. These characteristics plus those discussed in Paper I (namely, the strength of the He II emission and the hardness of the X-ray spectrum), provide convincing evidence that H0534−581 is an intermediate polar. As such, it has the longest spin period of any of the currently identified systems. The small mass function of the binary $(\sim 5 \times 10^{-3})$ implies that the inclination is $\lesssim 26°$ for a secondary star obeying the empirical mass-period relation. The inclination could be higher if the secondary mass is lower and the orbital period and $K$ velocity are higher, but it must still be less than $\sim 40°$. The behavior of the radial velocities, modulated at the spin period, can be explained as the superposition of two components produced in the rotating accretion funnels, or, alternatively, as a combination of many components arising from the accretion flow within the magnetosphere. We have argued that the system is unlikely to be diskless, because this would require an unacceptably high magnetic field. The only persistent photometric periods are the 6.5 hr orbital period and two puzzling short periods at ∼1938 and 2707 s. The latter period appears to be present in all the optical photometry. An *ad hoc* attempt has been made to explain these periods as arising from quasi-coherent "blobs" of optically thick material orbiting within the accretion disk at the Keplerian velocity. However, their origin is far from certain. The lack of detection of either the spin or orbital sideband optical periods may be a result of low system inclination coupled with a small dipole tilt.

We are grateful to Dayal Wickramasinghe for useful discussions and suggestions. We wish to acknowledge the excellent support of the AAO and ANU staff at Siding Spring Observatory. This work follows from a most successful collaboration with our colleagues Ron Remillard, Hale Bradt, and Dan Schwartz, involving the optical identification of weak *HEAO 1* X-ray sources, under the US/Australia Cooperative Science Program. Finally, D. A. H. B. acknowledges support through an ANU postgraduate scholarship.

## REFERENCES

Barrett, P., O'Donoghue, D., and Warner, B. 1988, *M.N.R.A.S.*, **233**, 759.
Bonnet-Bidaud, J. P., Mouchet, M., Buckley, D. A. H., and Tuohy, I. R. 1990, in preparation.
Buckley, D. A. H. 1988, Ph.D. thesis, Australian National University.
Buckley, D. A. H., and Tuohy, I. R. 1989, *Ap. J.*, **344**, 376 (Paper II).
Chanmugam, G., and Ray, A. 1984, *Ap. J.*, **285**, 252.
Chiapetti, L., *et al.* 1989, *Ap. J.*, **342**, 493.
Córdova, F. A., and Mason, K. O. 1983, in *Accretion Driven Stellar X-Ray Sources*, ed. W. H. G. Lewin and E. P. J. van den Heuvel (Cambridge: Cambridge University Press), p. 147.
———. 1984, *M.N.R.A.S.*, **206**, 879.
Drake, S. A., and Ulrich, R. K. 1980, *Ap. J. Suppl.*, **42**, 351.
Deeming, T. J. 1975, *Ap. Space Sci.*, **4**, 193.
Echevarria, J. 1988, *M.N.R.A.S.*, **233**, 513.
Faulkner, J. 1971, *Ap. J. (Letters)*, **170**, L99.
Greenstein, J. L., Sargent, W. L., Boroson, T. A., and Boksenberg, A. 1977, *Ap. J. (Letters)*, **218**, L121.
Hameury, J.-M., King, A. R., and Lasota, J.-P. 1986, *M.N.R.A.S.*, **218**, 347.
Hameury, J.-M., King, A. R., Lasota, J.-P., and Ritter, H. 1987, *Ap. J.*, **316**, 275.
Hellier, C., Mason, K. O., Rosen, S. R., and Córdova, F. A. 1987, *M.N.R.A.S.*, **228**, 463.
Horne, K., Wade, R. A., and Szkody, P. 1986, *M.N.R.A.S.*, **219**, 791.
Kaitchuck, R. H., Hantzios, P. A., Kakaletris, P., Honeycutt, R. K., and Schlegel, E. M. 1987, *Ap. J.*, **317**, 765.
Kaitchuck, R. H., Honeycutt, R. K., and Schlegel, E. M. 1983, *Ap. J.*, **267**, 239.
King, A. R. 1985, *M.N.R.A.S.*, **217**, 23P.
King, A. R., Frank, J., and Ritter, H. 1985, *M.N.R.A.S.*, **213**, 181.
Lamb, D. Q. 1983, in *Cataclysmic Variables and Related Objects*, ed. M. Livio and G. Shaviv (Dordrecht: Reidel), p. 299.
———. 1985, in *Cataclysmic Variables and Low-mass X-Ray Binaries*, ed. D. Q. Lamb and J. Patterson (Dordrecht: Reidel), p. 179.
Lamb, D. Q., and Mason, K. O. 1989, in preparation.
Lamb, D. Q., and Patterson, J. 1983, in *Cataclysmic Variables and Related Objects*, ed. M. Livio and G. Shaviv (Dordrecht: Reidel), p. 229.
Lamb, D. Q., and Melia, F. 1987, *Ap. Space Sci.*, **131**, 511.
Lubow, S. H., and Shu, F. H. 1975, *Ap. J.*, **198**, 383.
Lynden-Bell, D., and Pringle, J. E. 1977, *M.N.R.A.S.*, **168**, 603.
McHardy, I. M., Pye, J. P., Fairall, A. P., and Menzies, J. W. 1987, *M.N.R.A.S.*, **225**, 355.
Nauenberg, M. 1972, *Ap. J.*, **175**, 417.
Patterson, J. 1984, *Ap. J. Suppl.*, **54**, 443.
Patterson, J., and Raymond, J. C. 1985, *Ap. J.*, **292**, 535.
Penning, W. R. 1985, *Ap. J.*, **289**, 300.
Rappaport, J., Verbunt, F., and Joss, P. C. 1983, *Ap. J.*, **275**, 713.
Rosen, S. R., Mason, K. O., and Córdova, F. A. 1988, *M.N.R.A.S.*, **231**, 549.
Schmidt, G. D., Stockman, H. S., and Grandi, S. A. 1983, *Ap. J.*, **271**, 735.
Schneider, D. P., and Young, P. 1980, *Ap. J.*, **238**, 946.
Shafter, A. W. 1983, Ph.D. thesis, UCLA.
———. 1985, in *Cataclysmic Variables and Low-Mass X-Ray Binaries*, ed. D. Q. Lamb and J. Patterson (Dordrecht: Reidel), p. 355.
Shafter, A. W., and Targon, D. M. 1982, *A.J.*, **87**, 655.
Shafter, A. W., Szkody, P., and Thorstensen, J. R. 1986, *Ap. J.*, **308**, 765.
Shakura, N. I., and Sunyaev, R. A. 1973, *Astr. Ap.*, **24**, 337.
Stockman, H. S., Schmidt, G. D., Angel, J. R. P., Leibert, J., Tapia, S., and Beaver, E. A. 1977, *Ap. J.*, **217**, 815.
Stockman, H. S., Foltz, C. B., Schmidt, G. D., and Tapia, S. 1983, *Ap. J.*, **271**, 725.
Thorstensen, J. R., Wade, R. A., and Oke, J. B. 1986, *Ap. J.*, **309**, 721.
Tuohy, I. R., Buckley, D. A. H., Remillard, R. A., Bradt, H. V., and Schwartz, D. A. 1986, *Ap. J.*, **311**, 275 (Paper I).
Verbunt, F., and Zwaan, C. 1981, *Astr. Ap.*, **100**, L7.
Warner, B. 1983, in *Cataclysmic Variables and Related Objects*, ed. M. Livio and G. Shaviv (Dordrecht: Reidel), p. 155).
———. 1986, *M.N.R.A.S.*, **219**, 347.
Watts, D. J., Bailey, J., Hill, P. W., Greenhill, J. G., McCowage, C., and Carty, T. 1986, *Astr. Ap.*, **154**, 197.
Wickramasinghe, D. T. 1988, in *Proc. Vatican Conf. on Circumstellar Polarization*, in press.
Wickramasinghe, D. T., Stobie, R. S., and Bessell, M. S. 1982, *M.N.R.A.S.*, **200**, 605.

DAVID A. H. BUCKLEY: Department of Astronomy, University of Cape Town, Rondebosch 7700, Cape Town, South Africa

IAN R. TUOHY: British Aerospace Australia, P.O. Box 180, Salisbury, South Australia 5108, Australia